

# Naval Research Laboratory

Stennis Space Center, MS 39529-5004



NRL/MR/7240-94-7556

## Satellite Multisensor Data Techniques for Sea Ice Mapping

DENISE J. GINERIS

*Environmental Research Institute of Michigan  
Mississippi Office*

DOUGLAS A. MAY

*Remote Sensing Applications Branch  
Remote Sensing Division*

JEFFREY D. HAWKINS

*Prediction Systems Branch  
Marine Meteorology Division*

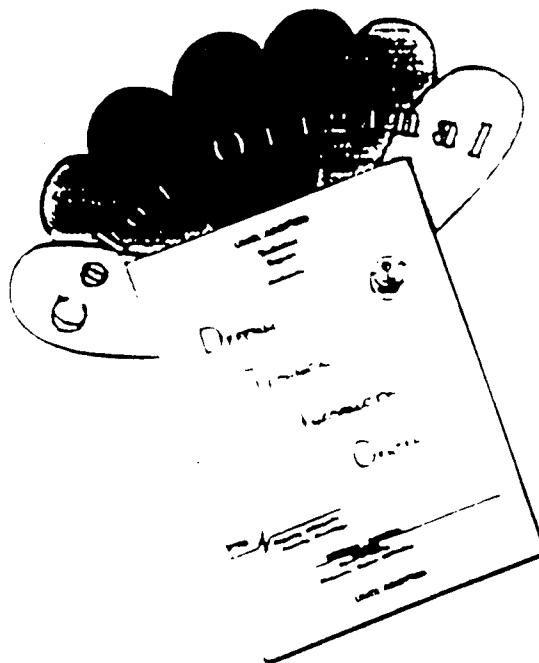


December 8, 1994

19950111 131

Approved for public release; distribution is unlimited.

# DISCLAIMER NOTICE



THIS DOCUMENT IS BEST  
QUALITY AVAILABLE. THE COPY  
FURNISHED TO DTIC CONTAINED  
A SIGNIFICANT NUMBER OF  
COLOR PAGES WHICH DO NOT  
REPRODUCE LEGIBLY ON BLACK  
AND WHITE MICROFICHE.

# REPORT DOCUMENTATION PAGE

Form Approved  
OMB No. 0704-0188

Public reporting burden for this collection of information is estimated to average 1 hour per response, including the time for reviewing instructions, searching existing data sources, gathering and maintaining the data needed, and completing and reviewing the collection of information. Send comments regarding this burden or any other aspect of this collection of information, including suggestions for reducing this burden, to Washington Headquarters Services, Directorate for Information Operations and Reports, 1215 Jefferson Davis Highway, Suite 1204, Arlington, VA 22202-4302, and to the Office of Management and Budget, Paperwork Reduction Project (0704-0188), Washington, DC 20503.

1. AGENCY USE ONLY (Leave blank)			2. REPORT DATE December 8, 1994	3. REPORT TYPE AND DATES COVERED Final
4. TITLE AND SUBTITLE  Satellite Multisensor Data Techniques for Sea Ice Mapping			5. FUNDING NUMBERS  Job Order No. 572519304 Program Element No. 0603207N Project No. X1596 Task No. Accession No. DN258025	
6. AUTHOR(S)  Denise J. Gineris*, Douglas A. May, Jeffrey D. Hawkins <sup>†</sup>			8. PERFORMING ORGANIZATION REPORT NUMBER  NRL/MR/7240--94-7556	
7. PERFORMING ORGANIZATION NAME(S) AND ADDRESS(ES)  Naval Research Laboratory Remote Sensing Division Stennis Space Center, MS 39529-5004			10. SPONSORING/MONITORING AGENCY REPORT NUMBER	
9. SPONSORING/MONITORING AGENCY NAME(S) AND ADDRESS(ES)  Space and Naval Warfare Systems Command 2451 Crystal Drive Arlington, VA 22202			11. SUPPLEMENTARY NOTES  *Environmental Research Institute of Michigan, Mississippi Office †Naval Research Laboratory, Marine Meteorology, Monterey, CA 93943-5006	
12a. DISTRIBUTION/AVAILABILITY STATEMENT  Approved for public release, distribution is unlimited.			12b. DISTRIBUTION CODE	
13. ABSTRACT (Maximum 200 words)  Operational sea ice mapping capabilities utilizing ground truth data are extremely limited due to the remote proximity and harsh environment of the polar regions. Satellite remote sensing offers a sufficient quantity of accurate, high resolution environmental parameters that satisfy many ice mapping requirements. This study explores the application of multiple satellite sensor data combination techniques for sea ice analysis. Sea ice information from visible, infrared, passive microwave, and active radar sensors are examined. The efforts focus on identification of individual sensor advantages and disadvantages and optimum combination of satellite sensor data sets for sea ice mapping. Each sensor's assets are exploited to increase the value of the collective whole by providing additional or collaborative ice feature information relative to other sensor data. Details of the satellite data set selection, the techniques utilized for combining and analyzing the data, and the results obtained are discussed. Results demonstrate that combination images of Advanced Very High Resolution Radiometer (AVHRR), Special Sensing Microwave/Imager (SSM/I), and altimeter data provide both ice feature detail and areal coverage in one image, making it easier for the user to take advantage of each data set at once and reinforce their confidence in the existence and location of specific ice features. Substitution of cloud contaminated AVHRR pixels with SSM/I ice concentration and or 85 GHz imagery, or red/blue/green combinations of visible, infrared, and microwave imagery produce the best combination results. Allowing the SSM/I ice concentration algorithms to vary above 100% also proved useful since correlations of these variations to the existence of new ice were observed. The difference of AVHRR channels 1 and 2 also provided the capability to delineate new ice and open water from other ice types in all regions. The altimeter ice index data provided most useful information at ice/water boundaries. Recommendations are also provided for future investigations.				
14. SUBJECT TERMS  SSM/I, Passive Microwave, Sea Ice, Water Vapor, Ambient Noise			15. NUMBER OF PAGES 52	
			16. PRICE CODE	
17. SECURITY CLASSIFICATION OF REPORT Unclassified	18. SECURITY CLASSIFICATION OF THIS PAGE Unclassified	19. SECURITY CLASSIFICATION OF ABSTRACT Unclassified	20. LIMITATION OF ABSTRACT SAR	

## Contents

1.0 Introduction .....	1
2.0 Multisensor Data Techniques.....	2
3.0 Data Selection .....	3
4.0 Results .....	5
4.1 Greenland Sea .....	5
4.2 Kara Sea .....	8
4.3 East Siberian Sea.....	11
4.4 Beaufort Sea .....	13
4.5 Regional Comparisons .....	14
5.0 Conclusions and Recommendations.....	15
6.0 Figures.....	18
7.0 Acknowledgments.....	49
8.0 References .....	50

Accesion For	
NTIS CRA&I	<input checked="" type="checkbox"/>
DTIC TAB	<input type="checkbox"/>
Unannounced	<input type="checkbox"/>
Justification _____	
By _____	
Distribution / _____	
Availability Codes	
Dist	Avail and / or Special
A-1	

## Satellite Multisensor Data Techniques For Sea Ice Mapping

### 1.0 Introduction

Environmental support spanning the earth's oceans is necessary for effective U.S. Navy operations. Many of the geophysical parameters that directly impact Navy operations are presently gathered via in situ measurements. The immense sampling areas involved however, often preclude adequate data collection via this method. Remote sensing by satellite offers a promising solution for acquiring accurate, high resolution parameters in sufficient quantity to satisfy many of the Fleet's needs. This fact is particularly true of operational sea ice mapping capabilities due to the remote locations and harsh environments associated with polar regions.

The Naval Ice Center (NAVCECEN) at Suitland, Maryland operationally generates charts that depict global ice edge, ice concentration, ice type, and iceberg locations throughout the Arctic and Antarctic Oceans as well as the Great Lakes region. The NAVCECEN coordinates a combination of limited resources to effectively provide for safe civilian and military operations within these harsh environments. Due to the remote proximity of the regions involved, satellite remote sensing data provides a wealth of information relative to the extremely limited ground truth data that is available. The NAVCECEN relies heavily on polar orbiting satellites due to the frequent polar coverage and their relatively large sensor spatial swaths. Several satellite sensors have been and are being used to operationally generate sea ice maps and fulfill forecast needs.

Each sensor has its distinct advantages and disadvantages, which serve to enhance or constrain its contribution to sea ice mapping. Table 1 depicts the advantages and disadvantages of each sensor type. Advanced Very High Resolution Radiometer (AVHRR) and Operational Linescan System visible and infrared satellite data, available from polar orbiting spacecraft, possess the advantage of excellent swath coverage, high spatial resolution (equal or less than 1 km at nadir), and the capability to discern ice concentration. Visible and infrared sensors provide excellent information on sea ice conditions when the images are cloud free. This limitation is significant since polar regions are often persistently cloud covered for several days or even weeks at a time. These sensors are of greatest use during daytime hours since ice/water discrimination is more easily detected by reflectance differences in the visible channels than infrared thermal contrast. Daytime data is not as readily available during the winter season, however, constraining the amount of sea ice information available during this important time period.

Passive microwave satellite data such as that available from the Special Sensor Microwave/Imager (SSM/I) sensor aboard the latest suite of Defense Meteorological Satellite Program (DMSP) satellites provides the advantage of a relatively large swath and a sensor that is neither limited by atmospheric weather conditions nor time of day. Passive microwave data have been used for many years to penetrate cloudy atmospheric conditions and permit "all weather" sensing of polar sea ice. Algorithms for ice concentration and ice type have been developed for the SSM/I channels. Ice concentration retrievals have proven to be relatively accurate; however, ice type algorithms have only demonstrated partial success in consistently discerning first-year and multiyear ice differences. SSM/I spatial resolution of 25 km is relatively coarse and creates problems when mapping ice edge, polynya, and near-shore ice locations.

Table 1. Sensor Advantages and Disadvantages

	AVHRR	SSM/I	Geosat	SAR	Grd. Truth	Combined Data
Swath	●	●	○	○	○	●
Resolution	●	○	●	●	●	●
All Weather	○	●	●	●	●	●
Day / Night	●	●	●	●	○	●
Ice Concentration	●	●	●	●	●	●
Ice Type	●	●	○	●	●	●

● = excellent    □ = moderate    ○ = poor

Active sensors are also very useful imaging systems in the polar regions. Altimeter data offers another all-weather sensor alternative. Altimeters have flown on Geosat, ERS-1, and TOPEX/POSEIDON. This study focuses on altimeter data obtained from the Geosat satellite. The sensor is extremely limited in swath coverage since the altimeter is bore-sighted and provides data only along the nadir track of the satellite. In addition, the satellite orbit is such that a data void exists poleward of 72° N. It has, however, proven its ability to detect the ice edge rather well by discerning the difference in signal between open water and ice. It has not been conclusively demonstrated, however, that any sea ice parameter other than ice edge can be reliably retrieved from altimetry on a consistent basis. Synthetic Aperture Radar (SAR) data also offers a high spatial resolution data set. The sensor is insensitive to weather conditions and time of day, and provides good results for ice concentration and ice type. However, SAR data swaths are very limited in spatial width. Unfortunately, no SAR data, coincident with other sensor data, was available at the time of this analysis.

It is readily apparent that combining the various satellite sensors can enhance an analyst's ability to confirm the information contained within any one individual sensor. Access to such a variety of data sets would allow the analyst to produce a more accurate sea ice map that details all desired parameters more clearly. This report explores the application of multisensor data techniques to operational sea ice mapping. This effort's focus is on how best to combine satellite sensor data sets to obtain optimum sea ice parameter information. Each individual sensor's advantages are exploited to increase the value of the collective whole. The ensuing sections of the report discuss the methods used to obtain and select the satellite data sets, the techniques used to combine and analyze the data, and a presentation of the results. Conclusions and recommendations for future investigations are provided.

## 2.0 Multisensor Data Techniques

Many data fusion techniques have been proposed by various researchers but often these techniques are tested only on one or two images, or are applied to only one region of the Arctic. This methodology, although fine for the development of new techniques, is not as appropriate from an operational standpoint. For operational purposes, techniques should be regionally and temporally invariant; a technique's ability to improve the analysis of data should not be dependent upon the region or season in which the imagery is collected. One goal of this report was to test the

applicability of multisensor data techniques to as wide a range of imagery as possible. Another goal of this analysis was to test those techniques that could be easily performed within the realm of operational ice mapping analysis. The best multisensor techniques for operational efforts are those that can be performed quickly, in order to meet the stringent deadlines under which ice analysis must be performed, and those which are simple to implement, enabling all ice analysts, independent of their level of computer skill, to use them. All techniques analyzed in this study are reasonably easy and quick to implement, provided the users have the ability to process data from different sensor sources to identical resolutions and projections. The latter point is key to improving sea ice mapping through sensor combination techniques.

The multisensor data enhancement techniques examined were divided into two groups: those that employed only multiple bands of AVHRR imagery, and those that employed combinations of AVHRR, SSM/I, and Geosat altimetry data. The calculation of ice concentration from AVHRR imagery has been established for some time (Emery 1991 and Steffen and Schweiger 1990), so most of the recent effort of AVHRR multichannel sea ice analysis has been in the development of algorithms, which delineate varieties of new, thin ice from older, thicker ice and open water. This delineation has been a difficult task, as thinner ice can take on appearances ranging from that of open water in the infrared to that of much thicker ice types in the visible bands. This can, in turn, cause the estimates of ice concentration from AVHRR to be in error. Two such efforts in recent years have been by Lee et al. (1993) and Massom et al. (1991). The method of Lee et al. (1993) involved the use of the visible and near-infrared channels of the AVHRR radiometer. By employing the difference between the reflectances of the visible data (channel 1, 585-685 nm) and the near-infrared data (channel 2, 713-1010 nm), they were able to enhance and discern new ice features that would normally be classified as open water in both individual visible and infrared images. Massom et al. (1991) employed the difference between the sums of the visible channels and the infrared channels (producing a result equal to  $[ch1+ch2]-[ch4+ch5]$ ) to enhance the variability and contrast among the thinner ice types. Both authors produced improved results with their methods, but testing was performed only on a small group (one to two) of images. In this analysis, these methods were tested on a larger group of imagery to see if they provided consistent improvement in ice characterization. These methods are referred to hereafter as the difference product and contrast product, respectively.

Other multisensor data techniques tested in this analysis employed comparisons of ice concentration and ice classification results from AVHRR, SSM/I, and Geosat sensors. The effect of data substitution was analyzed through combinations of AVHRR imagery and SSM/I ice concentration data. Cloud cover in the Arctic hides the ice surface from the visible and infrared channels of the AVHRR for long periods of time during the year. By applying a cloud mask to the AVHRR data and simply substituting the SSM/I ice concentration map for the cloud pixels, full coverage imagery, which retains the detail of the AVHRR data, can be obtained, allowing the operational user to more accurately produce maps of ice edge, ice concentration, and ice type. Red/green/blue composites of visible, infrared, and SSM/I data were tested to see if features in the ice pack could be differentiated through color coding. In addition, pixel-by-pixel comparisons of the results from the various sensor sources were also employed to see if a better characterization of sea ice could be achieved through the correlation of a number of sensors. It should be noted that time and spatial resolution differences between the different sensors, although minimized, make detailed quantitative comparisons somewhat inaccurate. Therefore, a more qualitative approach has been used in this report.

### 3.0 Data Selection

As AVHRR imagery is the staple of operational ice analysis, selection of test data was first driven by the availability of high quality AVHRR imagery. The main source of this imagery was a set of data collected for the Leads Arctic Research Initiative (ARI) program. The ARI AVHRR

data consisted of a set of sea ice imagery that was synoptic in both area and season. Images were graded according to arctic regional coverage and amount of cloud cover, and stored on digital tape at the Naval Research Laboratory's Remote Sensing Applications Branch. Ideally, an analysis, which included all of the arctic region for all seasons, was desired, but the level of effort required for this type of activity was well beyond the scope of this analysis. Instead, a smaller subset, consisting of data from the winter and early spring of 1989 was used. These seasons were selected because sea ice algorithms currently in use are thought to be more accurate during this period. AVHRR imagery for the multisensor test cases were then selected from this limited set of data based on the level of cloud cover. All of the test cases, except for one, were exceptionally cloud free. One cloudy case was included in order to test the feasibility of data substitution techniques. Beyond the issue of cloud cover, image selection was random, in hopes of achieving a data set truly representative of the quality of data that is handled operationally.

In order to achieve the desired high resolution coverage in the arctic region, the test cases were then processed to the most suitable of a series of projections, depending upon the region of cloud free coverage in each. These projections, covering the Kara/Barents Sea, Beaufort Sea, East Siberian Sea, and Greenland Sea, are illustrated in Fig. 1. Each projection appears as a separate box in the figure and has a nominal resolution of 0.015 deg/pixel (approximately 1.67 km/pixel), covering a region measuring approximately 1700 km by 1700 km.

It was then necessary to select high quality coincident data from other sensors. Data from the DMSP SSM/I, a passive radiometer operating at 19.4, 22.2, 37.0, and 85.0 GHz (with vertical and horizontal polarizations for all but the 22.2 GHz frequency), and the Geosat altimeter, were used for comparison. Imagery was chosen from these sensors that correlated as closely in time as possible to the overflights of the AVHRR sensor in order to minimize error introduced into the comparison by ice motion. On average, the difference in overflight time between the AVHRR and SSM/I sensors was 6 h, and that between the AVHRR sensor and the Geosat altimeter was 4 h. In some cases SSM/I data was available while Geosat data was not, and these cases were also included. In all, 11 test cases were taken into consideration: 1 in the Beaufort Sea, 1 in the Kara/Barents Sea, 3 in the Greenland Sea, and 6 in the East Siberian Sea. Table 2 provides a list of the test cases that were considered and the sensor data specifics. The data from the SSM/I and Geosat sensors were then processed to the AVHRR projections.

Table 2. Test Cases Used In Analysis

Region	Test Case	AVHRR Collection Time(Z)	SSM/I Collection Time(Z)	Geosat Collection Time(Z)
Kara Sea	25Feb89	09:17	00:35	01:55
Greenland Sea	22Jan89	15:05	06:01	06:13
	15Mar89	14:42	05:17	11:00
	20Apr89	13:34	06:05	12:23
East Siberian Sea	16Jan89	21:11	16:37	15:16
	25Jan89	20:26	17:17	15:37
	9Feb89	23:52	16:39	17:01
	2Apr89	20:49	16:44	20:05
	8Apr89	15:48	17:09	21:11
	11Apr89	23:37	16:31	21:18
	8Apr89	15:48	14:36	18:40

For the Geosat sensor an ice index was calculated from the energy in the time gates of the altimeter waveform response using the methods of Chase and Holyer (1990). These derived indices were found to have ice concentration accuracies of 16.0%. Other derivations of ice concentration from altimeter data could also be used for comparison, but this index was chosen because of its relatively high correlation to ice concentration. For the SSM/I sensor, ice concentration was calculated using both the Navy CAL/VAL and NASA algorithms, and images of the 85 GHz H brightness temperatures were also created. The SSM/I data was upsampled from a nominal resolution of 25 km to the resolution of the AVHRR imagery using the methods of Poe (1990). This algorithm uses an optimum interpolation technique to produce upsampled data while preserving the spatial resolution of the original data. Resampling the SSM/I data to match the AVHRR data was chosen over decreasing the resolution of the AVHRR data in order to maintain the delineation of lead features that can be easily identified in the AVHRR and Geosat data, but not as easily in the SSM/I data.

For both the multichannel and multisensor analyses, the techniques discussed in Section 2.0 were then applied to each image test case when applicable. Specific regions and ice conditions within the test cases where multisensor data combinations offered ice depiction improvement were analyzed. Overall image improvement was also noted. For the comparisons to altimeter data, individual image data was extracted from all sensors along the orbit nadir paths of the Geosat altimeter. The results of all comparisons were grouped according to region. Monthly variations in results were also examined when enough test cases existed within a region. For each region, the notable test cases are presented and a measure of the overall performance level of each multisensor technique within each region is provided. Arctic-wide performance was also tabulated. For all cases, the NAVICECEN ice charts were taken as ground truth, although these charts are only as accurate as the data used to generate them, and may have some inherent error. It should be noted that, while the number of test cases used in this analysis represents a four- or five-fold increase over the number of test cases usually used in the development of data fusion techniques, there are still too few cases to perform a seasonally variant comparison.

## 4.0 Results

### 4.1 Greenland Sea

The Greenland Sea region is represented by three test cases that span winter to early spring. An example of a typical test case and ice chart for this region during this season is presented in Figs. 2a and b. This region is characterized by a dynamic ice pack with general motion southward along the coast of Greenland. The ice pack consists of predominantly multiyear ice to the north, gradually changing to predominantly first-year ice in the south. Ice concentration within the pack is high, varying nominally from 100% in the north to no less than 80% in the south. The character of the ice pack is marked by loosely packed large floes in a matrix of open water leads, smaller floes, and new ice in the north and a dense pack of more uniform ice in the south. Occasionally, floes in the north are large enough to be documented in the ice charts, as is the case with the image from 22Jan89. The pack loosens up in an area just south of Scoresby Sound, creating lower ice concentrations in this area. Oden features extending from the ice pack also occur regularly east of the Greenland coast, and areas of ice streamers occur along the ice edge. Weather conditions for the test cases studied were quite similar. The coast of Greenland was fairly cloud free and winds were generally from the north to northeast with varying strength.

For this region of the Arctic, difference (AVHRR ch1-ch2) and high contrast (AVHRR [ch1+ch2]-[ch4+ch5]) products could be formed for two of the three test cases, 15Mar89 and 20Apr89. Visible data was not available for the 22Jan89 case. In both test cases, the difference product displays some very significant improvement over both the visible and infrared data. Most notable is the transparent nature of the clouds in this product for this area. The 20Apr89 test case is representative of the improvements (Figs. 3a through d). The entire ice edge is visible in the

difference product while clouds obscure some of the ice edge in both the visible and infrared data. The difference product also highlights an area of new ice streamers just east of Scoresby Sound, which is not easily observed in the single channel AVHRR data. The ice streamers have a much higher value in the difference product than the surrounding ice and open water. Within the pack just south of Scoresby Sound the difference product also helps to distinguish leads with new ice (bright features) from leads with open water (dark features) by utilizing the large difference between the visible and near-infrared returns of water and new ice in this area. The high contrast product appears to provide advantages of both the visible and infrared channels. This product is similar to the visible channels in that it provides high contrast between the ice and water, while also retaining the thermal contrast of different ice thicknesses from the infrared. This product does not, however, provide the reduction of cloud effects that the difference product provides. Similar effects could be achieved through the use of histogram equalization, but the contrast algorithm integrates information from four AVHRR bands, while histogram equalization is purely a modulation of the values in one band.

Figures 4a through f and Figs. 5a through f present comparisons of the AVHRR, SSM/I 85 GHz, and SSM/I ice concentration data for the 22Jan89 and 20Apr89 test cases. The NASA and Navy ice concentration algorithms have been allowed to vary above 100%. It will be demonstrated in following sections that these variations correlate well with ice type differences. Both Navy and NASA sea ice algorithms accurately locate the position of the ice edge for all test cases in the Greenland Sea region, with all ice concentration products generally showing the same trends along the Greenland ice pack. All total ice concentration charts show measurements of 80% to 100% ice concentration in the pack. In the 22Jan89 case, SSM/I ice concentration from both algorithms tends to increase to the south, which is the inverse of the trend in the NAVICECEN ice charts. The increase in the SSM/I total ice concentration may be linked to changing ice type or changing surface conditions along the Greenland coast. The 20Apr89 ice concentration map displays a decrease in ice concentration at Scoresby Sound, where a slight loosening up of the pack can be seen in the AVHRR data. The Navy algorithm total ice concentration values appear to be more variable in the north and more uniform in the south, mimicking the composition of the ice pack seen in the AVHRR, which appears to have a mixture of floes and open water in the north and more uniform ice in the south.

The NASA ice type algorithm also yields interesting results. All cases display multiyear ice concentration decreasing to the south and first-year ice concentration increasing to the south as in the NAVICECEN ice charts. The large multiyear floe highlighted in the NAVICECEN charts for the 22Jan89 test case can be seen in the SSM/I products as an area of significantly increased (from 40% to 60%) multiyear ice concentration and significantly decreased first-year ice concentration (from 50% to 10%). An anomalous patch of 50% multiyear ice concentration occurs in an area of predominantly higher first-year ice concentrations just east of Scoresby Sound in the 20Apr89 test case. This patch is correlated with an area of decreased brightness temperature in the 85 GHz data and with a uniform (without distinguishable floes) ice pack in the AVHRR (Fig. 3). Examination of the 19 GHz V, 19 GHz H, 37 GHz V, polarization ratio (PR), and gradient ratio (GR) for this area (area A), and for a comparable area with more consistent returns (area B) yields a higher polarization ratio and lower gradient ratio in the anomalous area (Table 3). The 19 GHz V brightness temperature is within 1 K for the two areas while the 37 GHz V and 19 GHz H brightness temperatures are decreased by about 10 K in the area of error. High polarization ratios due to decreased 19 GHz horizontal polarization brightness temperature may be caused by a small increase in the amount of open water in the area or the presence of new ice (Burns 1993). Since the gradient ratio is also different from one area to the other, differences in surface conditions may also be coming into play. The Navy ice type predominance algorithms identify the ice pack along the coast of southern Greenland to be predominantly multiyear ice, although the NAVICECEN ice charts and the NASA ice type algorithms indicate low concentrations of multiyear ice in this area.

Table 3. Comparison of Brightness Temperatures for the 20Apr89 Test Case

Area	MY%	Total Ice Conc.	TB19V	TB19H	TB37V	PR	GR
A	52.7	72.4	236.6	195.3	227.4	0.096	-0.0197
B	13.4	75.5	237.6	202.9	238.6	0.079	0.00197

In all Greenland Sea cases, especially the 22Jan89 test case, the 85 GHz data (Fig. 4f) provides details in the ice pack, such as the presence of large multiyear ice floes, and the transitions from a pack of ice floes in the north (low brightness temperatures) to a more uniform first-year ice pack in the south (high brightness temperatures). Different types of ice can also be distinguished in the 20Apr89 test case. The area of ice streamers mentioned previously has an extremely high mean brightness temperature. Just west of this feature is a distinct area of low mean brightness temperature that corresponds to an area of uniform ice in the visible and infrared data. Other areas of uniform ice in the pack do not exhibit these low brightness temperatures, so for this case, the 85 GHz data has added information that the AVHRR data does not provide.

Figure 6 displays a composite of AVHRR and SSM/I images for the 15Mar89 test case. In this case image thresholding has been used to remove the cloud contaminated AVHRR pixels and SSM/I Navy ice concentration data has been substituted. The integrated image provides both detail of the ice pack (from the AVHRR) and full coverage of the area (from the SSM/I). In addition, the use of the SSM/I data has improved the integrated image by providing information about the Oden event, which is indiscernible in the AVHRR. The SSM/I passive microwave does an excellent job of consistently discerning the Oden event, which is often undetectable in the visible and infrared channels due to clouds and/or the relatively low visible and infrared signature of the phenomena. The ice edge is well correlated between the two data sources, even when the difference in the time of collection is taken into account. It should be noted however, that the visible edge of the ice pack tends to correspond to the 30% or 40% contours of the SSM/I ice concentration. This correspondence has been observed in other studies as well (Cavalieri 1992).

Only one test case for the Greenland Sea region, 20Apr89, had sufficient Geosat altimeter data for comparison. Plots of data taken along the Geosat tracks illustrated in Figs. 3a and 8 are presented in Figs. 7a through c. Visible reflectance is plotted as percent reflectance times 10.0, SSM/I 85 GHz data as brightness temperatures in degrees Kelvin, and Geosat altimeter data in percent. Ice index values over land are invalid and should be ignored. All Geosat tracks which imaged the ice provided ice index responses that correlated to the ice pack, some more closely than others. Tracks that gave the best response were tracks B, D, and E. Track B crossed the ice pack to the south, where the other sensors indicated high concentrations of uniform first-year ice. A peak in the Geosat ice index of 80% corresponds to a region of ice just within the ice edge, which is easily identifiable in the AVHRR and 85 GHz data plots. An open water hole in the ice pack detectable in the AVHRR visible, infrared, and the SSM/I 85 GHz corresponds to a Geosat minimum of 9%. Tracks D and E cross the pack in the main area of interest in this test case, a location which contains the area of ice streamers and extremely low 85 GHz brightness temperatures. Track D crosses directly over the streamer area perpendicular to the main ice edge. The Geosat maintains a mean ice index of 30% until it encounters the area of ice streamers. At this location the ice index jumps to 94%. Within the ice streamer area, but just before the main ice edge, the Geosat ice index falls to 55%. Within the uniform ice area, which produces low SSM/I brightness temperatures, the Geosat values rise again to approximately 92%. Track E grazes the boundary between the ice streamer area and the main ice pack and then crosses the ice pack perpendicularly when the ice edge turns to the south. The ice index values maintain a high of close to 100% while the track grazes the ice streamer areas. The ice index value then dips to 45% just before the ice edge and then maintains a noisy mean value of about 70% over the rest of the ice

pack. Unfortunately, some of the noise jitter in the altimeter data is on the order of the variation in the ice response, which makes this measurement somewhat suspect for ice type and ice floe delineation. It does, however, correctly locate the ice edge for all cases.

Two examples of multisensor data combination techniques are presented in Figs. 8 and 9. Both examples illustrate two primary functions of data combination: data enhancement, which is the supplementation of one sensor's information by the use of another, and data validation, which is the corroboration of the information from one sensor by that of another. In Fig. 8, cloud contaminated pixels off the Greenland coast on the 20Apr89 test case have been removed from the AVHRR infrared imagery and replaced by SSM/I Navy algorithm ice concentration values. In this way, the AVHRR image has been supplemented with the SSM/I data. The resultant composite is an integrated product containing both the detail of the AVHRR and the coverage of the SSM/I. This composite image is then overlain with ice index estimates calculated from the Geosat altimeter. In this case the highest, most uniform Geosat ice index estimates appear to correspond to the area of ice streamers at the edge of the pack, while within the pack ice index values are more variable, perhaps mirroring the jumble of floes and water at that location. Geosat track E corroborates the ice edge information provided by the SSM/I as evidenced by the elevation of ice index values when the ice edge is encountered. Track D helps to define the location of the water/ice boundary better than the infrared data alone. Combining data from multiple sensors readily assists the analyst's ability to confirm the existence and location of various features.

In Fig. 9 a red/green/blue composite is formed by directing SSM/I 85 GHz, AVHRR visible, and AVHRR infrared data, respectively, to the red/green/blue channels of a monitor display with equal weighting. Using this technique, different features in the image are characterized by different hues and intensities. In this case, the clouds are mainly lavender and orange, the open water, dark red, and the ice pack, shades of green. In the ice streamer area, at least four different hues are observed: the dark red of the streamer area, the dark orange of the new ice area south of the streamers, the blue green of the uniform pack west of the streamers, and the yellow green of the main part of the pack. Changes in 85 GHz brightness temperature provide most of the subtle color variations in the ice pack, while the visible and infrared data provide the detailed resolution in the composite and the large-scale color differences segmenting ice, water, and clouds.

#### 4.2 Kara Sea

Only one test case exists for the Kara Sea region, an image collected in late winter on 25Feb89 (Fig. 10a). NAVICECEN ice charts (Fig. 10b) show the Kara Sea to be covered exclusively by first-year and young ice. To the west, the Barents Sea contains first-year and new ice to the north and open water in the south. The ice edge runs close to the coast of Russia and the southern half of Novaya Zemlya and cuts east to west through the Barents Sea. Large regions of exclusively new and young ice exist along the southeastern coast of Novaya Zemlya and along the eastern coast of the peninsula just south of Novaya Zemlya. The ice pack in the north Barents Sea and Kara Sea contains many lead features. Clouds exist in the southwestern portion of the image associated with a low pressure system centered just east of Finland (according to available weather charts). Winds are predominantly light and variable in the Kara Sea, with extremely cold air temperatures averaging -25 °F in the region. Areas of ice analysis interest within this region are the southern section of the Kara Sea within the curve of Novaya Zemlya, the ice edge, and the pack ice south of the islands of Spitzbergen and Franz Josef Land.

For this image, both visible and infrared data were available (at least for the southern half of the image) so tests of the difference and contrast algorithms could be performed. Image results of these algorithms are presented in Figs. 11a through d in comparison to visible and infrared data for the same area. Along the ice edge some improvement is achieved, with the difference algorithm highlighting new ice at the ice edge. A polynya along the fast ice southeast of Novaya Zemlya is

enhanced and delineated from open water. This feature appears to have very similar albedoes and temperatures to that of open water in both the visible and infrared data, but the difference image has brighter returns in this area than the open water (albedo difference of ice = 7.00, albedo difference of water = 1.83), indicating that the visible data is brighter than the near infrared data in this area, as would be expected for ice (Grenfell and Perovich 1984). The difference product also discriminates differences in new ice. Three different ice types are detected within one of the new ice areas in the Kara Sea on the east coast of Novaya Zemlya. These types are indistinguishable in ch1 and ch4. There is not sufficient dynamic range in the visible data in the northern part of the image to make the difference product useful for the whole image.

The contrast product is not a significant improvement over results obtained from the infrared channels in this case because the visible values are very small. The product results in what is essentially an inverted infrared image. The product does, however, tend to increase the contrast of the image, as evidenced by the increased coefficients of variation calculated for areas 1, 2, and 3 in the image (Table 4). The coefficient of variation, which is the ratio of the standard deviation of an area and its mean, provides a measure of the variability within a region independent of the mean value of the region; that is, it provides a measure of relative variability among areas.

Table 4. Comparison of Coefficients of Variation for the Kara Sea Test Case

Area	Original Coef. of Variation	High Contrast Coef. of Variation
A	0.22	0.27
B	0.13	0.20
C	0.13	0.21

Some intriguing results are obtained from the SSM/I ice concentrations (Figs. 12a and b) when compared to the AVHRR imagery (Fig. 10a). The infrared imagery shows two areas of thinner ice (the darker gray areas) along the southeastern coast of Novaya Zemlya. When the SSM/I Navy and NASA ice concentration algorithms are allowed to vary above 100%, the areas represented by the variations above 100% appear to coincide with the areas of thin, new ice in the infrared imagery. The responses of the SSM/I algorithms, however, differ from each other in these areas. The Navy algorithm produces values of 120% for most of the Kara Sea, with the new ice areas producing values 10% to 15% below these values. A high of 130% is achieved in the center of the south Kara Sea, which can be correlated to an area of low brightness temperatures in the 85 GHz image but has no correlation in the infrared imagery. For these same ice areas the NASA algorithm varies inversely. Lower concentrations occur in the center of the southern Kara Sea, with increases of about 25% in the new ice areas. The NASA multiyear and first-year concentration results (Figs. 12c and d) indicate low to no amounts of multiyear ice in the area and extremely high amounts of first-year ice in the region. In the new ice areas detected in the infrared imagery, the first-year concentrations increase to a maximum of 100%. The Navy ice type predominance algorithm (Fig. 12e) provides results consistent with the NAVICECEN ice charts everywhere except along the ice edge and around Spitzbergen. This contrasts with the more inaccurate results obtained in the Greenland Sea and demonstrates regional inconsistency in the Navy ice type predominance algorithm. The presence of multiyear ice on the ice edge may be an artifact of the interpolation used to produce the image. The Navy total ice concentration algorithm appears to be more sensitive to the variations in this area than the NASA ice concentration images and, on average, produces higher concentrations than the NASA algorithm. The variations in the Navy total ice concentrations may be attributed in part to variations in surface roughness or snow cover in the area. Burns (1993) showed similarities between the total ice concentration calculated with the Navy algorithm and the 37 GHz H brightness temperature, which is sensitive to snow and surface roughness. The Navy ice concentration algorithm is linearly related to the 37 GHz H brightness temperature for those cases where clouds are not significant, while the NASA algorithm

does not employ the 37 GHz H channel in its calculations. Variations in the Navy ice concentration values above 100% are expressed in the NASA algorithm as variations in first-year and multiyear ice concentrations. Some of these variations can also be seen in the lee of Spitzbergen and Franz Josef Land, but the effect here may be due to water vapor emanating from a polynya along the fast ice zone. The NASA algorithm also shows multiyear ice occurring in open water areas of the Barents Sea.

Anomalous NASA ice concentration values are calculated in the center of the south Kara Sea where multiyear concentration peaks at 30%. This area should be entirely first-year ice since the Kara Sea melts completely each summer, and weather patterns prior to this time make it unlikely that multiyear ice could have been advected into the region. Table 5 presents the mean brightness temperature measurements for the individual 19 GHz V, 19 GHz H, and 37 GHz V radiometer channels as well as the mean polarization and gradient ratios calculated for three areas (A, B, and C) within the Kara Sea. These areas were selected because they all appear to be approximately 100% first-year ice with no leads in the AVHRR imagery (Fig. 11b) and correspond to NASA multiyear ice concentration values of 31%, 13%, and 3%, respectively. In all cases, total ice concentration calculated from the NASA ice algorithm is approximately 97% (increasing slightly from 96% to 98% with increasing multiyear concentration). The 19 GHz V and 19 GHz H returns are fairly constant among the sample areas, while the 37 GHz V return shows a difference of over 10 K between sample A (highest multiyear concentration) and sample C (lowest multiyear ice concentration). The low of 241 K for sample A is not consistent with the range of brightness temperatures that would be expected from first-year ice (Steffen and Schweiger 1989). This drop in the brightness temperature of the 37 GHz vertical polarization frequency without a drop in the 19 GHz frequency values could be due to the presence of an aged snow cover on the first-year ice (Cavalieri 1992). Given the late February time frame for this image, the presence of an aged snow cover in this region is a distinct possibility.

Table 5. Comparison of Brightness Temperatures for the Kara Sea Test Case

Area	MY%	Total Ice Conc.	TB19V	TB19H	TB37V	PR	GR
A	30.7	98.1	256.0	239.0	241.4	0.0343	-0.0293
B	13.0	97.4	256.9	239.4	248.9	0.0353	-0.0158
C	3.4	96.1	258.0	241.3	252.3	0.0334	-0.0112

Both SSM/I 85 GHz and AVHRR sensors easily detect the ice edge and new ice areas in the southern Kara Sea (Figs. 10a and 12f). Around Spitzbergen and Franz Josef Land the visible detector does not have sufficient dynamic range to distinguish different ice types, but leads, floes, and possible areas of new ice are readily apparent in the 85 GHz SSM/I imagery and in the AVHRR infrared imagery. This demonstrates that the spatial resolution of the 85 GHz data provides significant ice mapping information that may not be available at the lower SSM/I frequencies and in the AVHRR if cloud cover exists.

The enhancement of sea ice mapping with Geosat ice index estimates is explored through the comparisons of sensor response given in Figs. 13a and b, and illustrated in Fig. 10a. Each set of plots represents a comparison of altimeter, SSM/I, and AVHRR data taken along a Geosat orbit track. In the 25Feb89 Kara Sea image, two Geosat tracks were collected, both of which cross the southern Kara and Barents Seas east to west (Fig. 10a). In Figs. 13a and b, AVHRR infrared data is plotted as 500 minus the value in tenths of a degree centigrade (the data is inverted), SSM/I 85 GHz data as brightness temperatures in degrees Kelvin, and Geosat altimeter data in percent. Both Geosat tracks are noisy, but Geosat ice index values still appear to correlate to ice/water boundaries and to areas of new ice. In track B this effect can be noted on either side of the Kara Sea. On the west side, a large area of new ice produces ice index values of approximately 86% while on the

east side, an area of leads visible in the infrared produces ice index values of approximately 75%. Ice index values appear to have a mean value in the other areas of the Kara Sea of about 55%, but the values fluctuate significantly about this mean. Track C displays similar results. In the region of new ice in the Kara Sea the Geosat altimeter produces ice index values of 93%. It is interesting to note that the Geosat ice index plot registers a slight increase in that region of the Kara Sea that produces erroneously high NASA algorithm multiyear ice concentrations. As the altimeter is unaffected by weather conditions, this increase supports the theory that the source of the discrepancy may be due to surface scattering differences in the ice. Snow cover, as proposed previously, could be responsible for such differences. For this test case, the altimeter easily discerns the ice/open water boundary and, less significantly, the existence of new ice. Due to sensor noise, however, the detection of ice leads by altimeter data alone, is inconsistent. However, by combining the infrared and altimeter data as shown in Fig. 10a, the analyst is provided with additional information that can support or confirm the location and existence of specific ice conditions. Ice index values over land are invalid and should be ignored.

#### 4.3 East Siberian Sea

The East Siberian Sea region contains the largest number of test cases: there are six in all, spanning a period in time from the middle of January 1989 to the middle of April 1989. An example of a typical test case and ice chart for this region during this season is presented in Figs. 14 a and b for 9Feb89. The region is characterized by a mixed ice pack of multiyear and first-year ice with a fast ice zone along the coast. In the western part of the image, fast ice extends up to 800 km into the sea. Progressing eastward along the coast, the fast ice tapers to a minimum of about 25 km in width at Chayunskya Guba ( $170^{\circ}$  E), and beyond this point, maintains an average width of about 30 to 40 km. The area along this fast ice boundary is extremely dynamic, with polynya formation and refreezing occurring frequently, especially along the thicker fast ice area and directly north of Kolyuchinskya Guba ( $174^{\circ}$  W). During January and February, the ice charts indicate that the entire region, excluding the fast ice edge, is 100% ice covered with predominantly multiyear ice (a 9:1 ratio of multiyear to first-year ice). In April, a region of first-year ice developed north of the New Siberian Islands. The central East Siberian Sea has a well developed lead system throughout the time period analyzed. All test cases except for the data from 9Feb89 and 8Apr89 are mostly cloud free. Weather conditions in the region for January and February cases were dominated by relatively strong high pressure systems centered over Siberia. Temperatures were significantly cold, ranging from  $-35^{\circ}$  to  $-45^{\circ}$  F with winds light and predominantly westerly. The April cases demonstrated relatively milder temperatures of  $-20^{\circ}$  to  $-30^{\circ}$  F with light winds generally from the southwest or south.

Visible data was only available for two of the East Siberian test cases, 2Apr89 and 11Apr89. Of these two test cases, one was collected by NOAA-10 and the other had magnetic tape parity errors while processing, so channel 5 data, and hence, the high contrast product was not available for either. Both test cases do provide, however, a good test of the AVHRR difference product. Comparisons of the difference product, visible image, and infrared image for the 11Apr89 test case are presented in Figs. 15 a through c. This image is characterized by a relatively large area of new ice north of the thickest fast ice zone, and by several large and small leads throughout the image. The detection abilities of the difference product can easily be seen in the area of new ice. In both the visible and infrared imagery this area appears to be very uniform, which would indicate the existence of one ice type. In addition, the northern boundary of this area is not well defined, probably due to water vapor effects. In the difference product, several different types of returns can be seen within this new ice area, indicating the existence of varying thicknesses of ice. The northern boundary of the region is also better defined. Another advantage of the difference product can also be observed throughout the lead field in the region. The leads appear as dark linear features in the visible and inverted infrared imagery. In the difference product, however, these same leads can appear either dark or bright, indicating the existence of open water or new ice in the lead, respectively. The reason for this delineating ability is that the

albedo of ice is significantly less in the near infrared frequencies than in the visible frequencies (Grenfell and Perovich 1984) while the albedo of water in the two frequency ranges is similar (Lee et al. 1993). This would cause open water areas to appear dark in the difference image while new ice areas would appear bright. The ability of the difference product to define new ice types and discern new ice from open water is also apparent in the 2Apr89 image but to a lesser extent, due to the increased cloudiness and lesser amount of dynamic range in the visible channels on this image.

Representative SSM/I results typical of the region are presented in Figs. 16 a through f, and illustrate the 85 GHz, NASA algorithm, and Navy algorithm results for the test case of 9Feb89. Ice charts for 7Feb89 show the area to contain 90% to 100% ice cover throughout the region with 90% multiyear ice in the center of the East Siberian Sea and 90% to 100% first-year ice along the coast. Both the Navy and NASA algorithms indicate total ice concentrations of 90% and higher for most of the region, with the NASA algorithm being generally less variable than the Navy algorithm. Both algorithms indicate lower concentrations of 60% on the far east side of the coast, in an area where polynyas occur frequently. The Navy ice type predominance algorithm shows a large area of multiyear ice in the central East Siberian Sea, but this area does not encompass as large an area as indicated by the ice charts. The NASA multiyear and first-year maps indicate up to 100% first-year ice along the coast and in the west side of the image, and primarily 50% to 90% multiyear ice in the east side of the image. A distinct boundary separates the image into a predominantly multiyear half and a predominantly first-year half. This boundary is also very apparent in the 85 GHz data as high brightness temperatures (approximately 220 K) in the west and low brightness temperatures (approximately 180 K) in the east although there is no evidence in the ice charts that such a multiyear / first-year delineation exists. In addition, there is no indication in the AVHRR that there is any difference in the ice or weather effects across the boundary. Table 6 provides the 19 GHz and 37 GHz brightness temperatures and the polarization and gradient ratios for the areas marked A and B in Figs. 14 and 16. The slight increase in total ice concentration and significant decrease in the multiyear concentration from the eastern side of the sea to the western side of the sea are comparable to the expected changes due to weather effects predicted by Maslanik (1992). Given the vapor effects present in the AVHRR image north of the New Siberian Islands, the SSM/I returns in the region may be affected by vapor emanating from the fast ice edge and leads in the area. The fact that this boundary feature is apparent in the microwave data to varying degrees in the other East Siberian test cases, as well as in some of the NAVICECEN ice charts from January and February, however, points to an actual ice type difference across the area. Differences between multiyear and first-year ice types should not cause the differences in the NASA total ice concentration values seen here, but the presence of thin ice in newly frozen leads, or of other ice types, may cause errors in the NASA ice concentrations. Perhaps a mixture of these two effects is acting to modulate the SSM/I brightness temperatures in the area.

Table 6. Comparison of Brightness Temperatures for the 9Feb89 Test Case

Area	MY%	Total Ice Conc.	TB19V	TB19H	TB37V	PR	GR
A	1.3	100.0	250.6	236.3	244.4	0.0293	-0.0125
B	89.8	94.8	235.4	212.9	201.4	0.0504	-0.0779

The comparison to Geosat altimeter ice index data yielded mixed results for this test region. The plots presented in Figs. 18 a through c for the tracks illustrated in Fig. 17 for the 25Jan89 test case are representative of the type of results that have been achieved. When correlation of the Geosat ice index data to AVHRR or SSM/I is observed, it is usually represented as increased ice indexes in regions of new ice or leads. In the plot for track C an increase in the Geosat ice index appears well correlated to a new ice area off of the edge of the fast ice. Track B, however, which crosses the same new ice area, does not show any significant increase. Similarly, some areas of

leads are detected by the Geosat altimeter, as in track B, while others are not, as in track C. These contradictions in detection are apparent in all cases for this region. Because of the variability in the response of the Geosat, it does not appear to be a very effective tool here.

#### 4.4 Beaufort Sea

The test case for the Beaufort Sea was collected on 8Apr89 (Figs. 19 a and b). This test case represents conditions in the Arctic when cloud cover and darkness renders the use of AVHRR sensor difficult. The northern half of the image contains pack ice with a network of leads, all of which is covered by a layer of thin clouds. The southern half of the image is completely cloud covered. The NAVICECEN ice charts show the area to be covered with 90% to 100% ice with multiyear and first-year ice in a ratio of 9:1 down to 72° N. Below 72° N ice coverage is also 90% to 100%, but the composition is uncertain. Weather charts show warm air streaming northward from the Pacific, generating the large cloud mass in the region.

The visible AVHRR data was unavailable due to darkness so test of the difference and high contrast products could not be performed. No Geosat tracks were available for this day either, so multisensor data enhancement, in this case, is whatever enhancement can be provided by a combination of infrared AVHRR and SSM/I data. Figures 20 a through f present the SSM/I ice concentration results and SSM/I 85 GHz brightness temperatures for this area. The 85 GHz image shows significant weather effects, although highs in brightness temperature along Banks Island (125° W) and the north coast of Alaska are somewhat consistent with areas of 40% to 60% new and young ice in the NAVICECEN ice chart. A lower brightness temperature along the north of Cape Lisburne (165° W) also correlates with an area of reduced concentration in the ice charts. The uncapped Navy algorithm ice concentration image also displays patterns and features similar to the NAVICECEN ice chart. Along Banks Island and the north shore of Alaska the ice concentration values drop to a low of 100% from an average of 120% elsewhere in the arctic region. This trend is similar to that of other Navy ice algorithm images, where a concentration greater than, but close to, 100% appears to be correlated to new or first-year ice. A low of 80% is reached off of Cape Lisburne, which may correspond to the area of 70% to 90% first-year and young ice in the ice charts. Weather effects are also not apparent in the NASA total ice concentration image, although Maslanik (1992) predicts a slight increase in the total ice concentration due to weather effects. The relatively sharp decrease in multiyear ice concentration (and corresponding increase in first-year ice concentration), which occurs at about the same geographic location as the edge of the heavy cloud layer, can probably be attributed to weather effects, although the first-year/multiyear ice boundary for this region is also in this area.

Figure 21 shows a composite AVHRR and SSM/I image. In this image the clouds in the AVHRR data have been masked using a simple bilevel threshold and SSM/I Navy ice concentration data has been substituted. This image illustrates how easily data from two sensors can be combined to produce an improved image. The AVHRR data provides the detail in this case, while the SSM/I, though not having fine resolution, can be used to provide some measure of ice concentration where the AVHRR provides no information at all. The user could also substitute SSM/I 85 GHz channel information that would provide slightly better spatial detail than the ice concentration product.

#### 4.5 Regional Comparisons

Since test cases from several arctic regions were examined, some general comparisons and conclusions can be made regarding the regional effectiveness of various data combination techniques for sea ice mapping. In general, the visible and infrared imagery provide valuable information on ice edge, ice floe locations, leads and new and fast ice detection in all regions. Both types of data are limited however by cloud cover that can be extensive for periods of time in the Arctic. The visible data is further limited by the amount of daylight, which is minimal during the arctic winter when ice is forming and increasing in quantity. Use of the AVHRR channel 1 minus channel 2 difference technique effectively delineates new ice and open water from other ice types in all regions, provided that the visible reflectance data is of sufficient dynamic range.

SSM/I passive microwave data can be exploited most effectively by using the 85 GHz data. This channel provides the greatest spatial resolution and effectively defines the general ice pattern in nearly all weather conditions except during heavy precipitation. The 85 GHz brightness temperature delineates the ice edge, new ice areas, large ice floes and broad leads quite well in all regions. The 85 GHz brightness temperature also appears to correlate weakly with first-year and multiyear ice differences. This was most noticeable in the East Siberian and Greenland Seas.

SSM/I ice concentration algorithms were found to be sensitive to new ice regions. Both the Navy and NASA algorithms demonstrated a correlation between the variability of ice concentration values above 100% (uncapped) and the presence of new ice. The Navy algorithm displayed a decrease in uncapped total ice concentration in areas of new ice while the NASA uncapped total ice concentration algorithm showed a slight increase. The correlation was much more noticeable in the Navy ice concentration estimates than in the NASA ice concentration estimates. This was best observed in the Kara and East Siberian Seas. Both algorithms depicted open areas in the Beaufort Sea and defined the Oden events that occur in the Greenland Sea. The Navy ice concentration estimates appeared more spatially variable than the NASA ice concentration estimates in all regions examined. This increased variability is probably due to the dependence of the Navy ice concentration algorithm upon the 37 GHz H brightness temperatures in cloud free cases. Burns (1993) has observed striking similarities between the Navy ice concentration algorithm estimates and 37 GHz H brightness returns in the Antarctic and has suggested that variability in the Navy ice concentration estimates may, in fact, be linked to the 37 GHz H channel's sensitivity to snow and surface conditions. Variability in the Navy ice concentration estimates may also be due to variations in surface temperature, since the Navy algorithm does not employ brightness temperature ratios in its calculations, which would serve to mitigate temperature differences. The Navy algorithm also appeared to produce, on average, slightly higher total ice concentration estimates than the NASA algorithm for concentrations of ice above about 70%. Below 70% the results are comparable, though not identical. Water vapor effects appeared to cause little error in either the Navy or NASA total ice concentration estimate. A future comparison of algorithm results to ground truth is really necessary for the variations in the ice concentration estimates of either algorithm to be fully understood.

With regards to ice type classification, the NASA algorithm provided generally more consistent results. Although the Navy algorithm appeared to perform better in the Kara Sea, it was entirely wrong in the Greenland Sea and inconsistent in the East Siberian Sea. The Navy algorithm also demonstrated problems with ice classification along coastal locations and ice edges in all regions. Although the NASA algorithm was typically accurate for all regions, it demonstrated increased first-year concentrations that were consistently high in areas of new ice. The NASA algorithm also depicted high percentages of multiyear ice in first-year or new ice regions like the Kara Sea and Oden events in the Greenland Sea. Such occurrences are thought to be related to ice surface condition changes caused by snow cover and melting. The presence of water vapor also

appeared to cause some error in the NASA first-year and multiyear ice percentages. Surface and air temperature fluctuations may also be coming into play (Maslanik 1992).

Geosat altimeter data consistently demonstrated good detection of open water and ice boundaries in all regions. Although the altimeter data often correlated well with new ice and ice lead locations, the number of noncorrelations was also significant in each region. Thus, the best application of altimeter data in the Arctic appears to be for ice edge detection. It should be noted that only the ice index formulation of Chase and Holyer (1990) has been tested in this analysis. Other ice index formulations or altimeter parameters may be more sensitive to different ice features.

## 5.0 Conclusions and Recommendations

Table 7 provides a synopsis of the results of this study. In the table, the improvements that a particular multisensor data enhancement provides in a given region are measured on a scale of 1 to 5 with 1 being equal to little improvement and 5 being equal to great improvement. The table thus provides a measure of the usefulness of each technique to the operational community, based on the analysis of these test cases. Techniques which rate highly should be incorporated into normal operating procedures. Techniques which rate lowly can be used in situations where an operator has exhausted more useful possibilities. Techniques which could not be tested are listed with an N/A (not available). Ratings of single channels of data are for the benefit these channels add to a multisensor comparison.

Table 7. Applicability of Multisensor Data Enhancement Techniques

Region	AVHRR VIS	AVHRR IR	Difference	High Contrast	Uncapped SSM/I	85 GHz	Geosat
Kara	3	4	3	1	4	4	3
Greenland	4	4	4	2	4	4	3
E.Siberian	4	4	4	1	4	4	1
Beaufort	N/A	1	N/A	N/A	4	3	N/A
All	4	4	4	2	4	4	2

As can be seen from the ratings, there are no perfect techniques that are both extremely informative and reliable. There are, however, several techniques that tested well enough over a wide range of regions that they should be considered for operational use. First among these techniques is the combination of SSM/I imagery, both 85 GHz response and ice concentration, with AVHRR data. As shown in case after case with few exceptions, the SSM/I sensor provides relatively cloud free, accurate ice concentration and ice type results when compared to the AVHRR. Increased spatial resolution in the SSM/I data can be achieved through the incorporation of 85 GHz brightness temperatures. The difference of AVHRR channels 1 and 2 also proved to be a useful tool for most regions where visible data was available. The altimeter ice index data provided useful and somewhat consistent sea ice information, especially at ice edges. However, this sensor is severely limited by its spatial coverage, which is along the satellite nadir track only. The incorporation of the high contrast AVHRR product into the analysis of the imagery does not appear to consistently provide assistance and should be considered a secondary technique. Although each individual technique has limitations, a combination of the highest rated techniques provides ice mapping information that is superior to the information available from a single sensor. Thus, operational sea ice mapping can be enhanced by the utilization of multiple sensor data in any given region.

Recommendations for use of these multisensor data techniques by the operational community are to:

- incorporate the SSM/I 85 GHz brightness temperatures into the sea ice analysis. Although this frequency is the most sensitive to weather effects, it is also the most sensitive to changes in ice type and has the highest resolution. For these reasons, the 85 GHz data should be used in sea ice analysis either alone or as part of an improved sea ice algorithm. The 85 GHz channel consistently demonstrated the ability to discern ice type in the regions examined, weather permitting. The 85 GHz data is also very beneficial in the marginal ice zone and along the ice edge, since it allows the discrimination of smaller spatial scale features that are not readily apparent in the SSM/I ice concentration image results.
- take the cap off the ice concentration values generated by the Navy SSM/I sea ice algorithm. It has been demonstrated that there is a link between the existence of thin new ice areas in the AVHRR and variations in the Navy ice concentration above 100% for all regions of analysis. As the Navy SSM/I sea ice algorithm does not provide ice concentration by type, and as the type predominance algorithm has demonstrated errors, these variations can be used as indicators of possible new ice areas.
- include the results of the NASA SSM/I sea ice algorithm as part of the daily operational analysis. The NASA total ice concentrations appear to be relatively accurate when compared to NAVICECEN ice charts. The NASA algorithm also provides estimates of multiyear and first-year ice concentrations, which the Navy algorithm does not provide. These estimates should be taken into account as an extra source of information when ice analysis is performed. It should be noted that the ice charts are only as accurate as the data used to generate them and may have some inherent error.
- produce combination images of AVHRR and SSM/I ice concentration. These images may be red/blue/green combinations of SSM/I and AVHRR, or may be of AVHRR imagery with SSM/I data substituting for cloud contaminated pixels. Either way, an image is produced in which the AVHRR data provides detail and the SSM/I provides coverage, making it easier for the user to take advantage of both sets of data and reinforce their confidence in the existence and location of specific ice features.
- use other data combinations such as the difference product, high contrast product, and AVHRR enhanced with altimeter data products, when available, to improve the characterization of new ice. It should be noted that these techniques and combinations are not foolproof for all regions and seasons, and sometimes do not provide any improvement. The difference product appears to have the most consistent results, delineating new ice and open water from other ice types in all regions.

It is apparent that a combination of data sources does improve the quality of ice interpretation and that the use of multisensor data techniques described in this report should be pursued. Some issues that should be addressed in any future work in this field are the following:

- better data registration. Before any quantitative improvements using satellite imagery data can be made, the data must be accurately registered. Ice motion between images must also be taken into account.
- improved weather screening for the SSM/I imagery. Eighty-five GHz data provides relatively high spatial resolution for a microwave sensor, however this frequency is significantly affected by weather. Development of effective weather screening algorithms would improve the accuracy and usefulness of the 85 GHz data for future data comparisons.

- the incorporation of SAR data into the multisensor study. SAR, with its inherent all-weather capabilities and fine resolution, is good at distinguishing ice types and estimating ice concentration.
- experiments to supply ground truth. This would serve to validate the methods, making them more useful, and might aid in the development of other techniques.
- investigations into more intensive sensor combination techniques such as principal component analysis. Such combination techniques may be able to provide unique multisensor ice parameters unachievable with single sensor studies.

## **6.0 Figures**

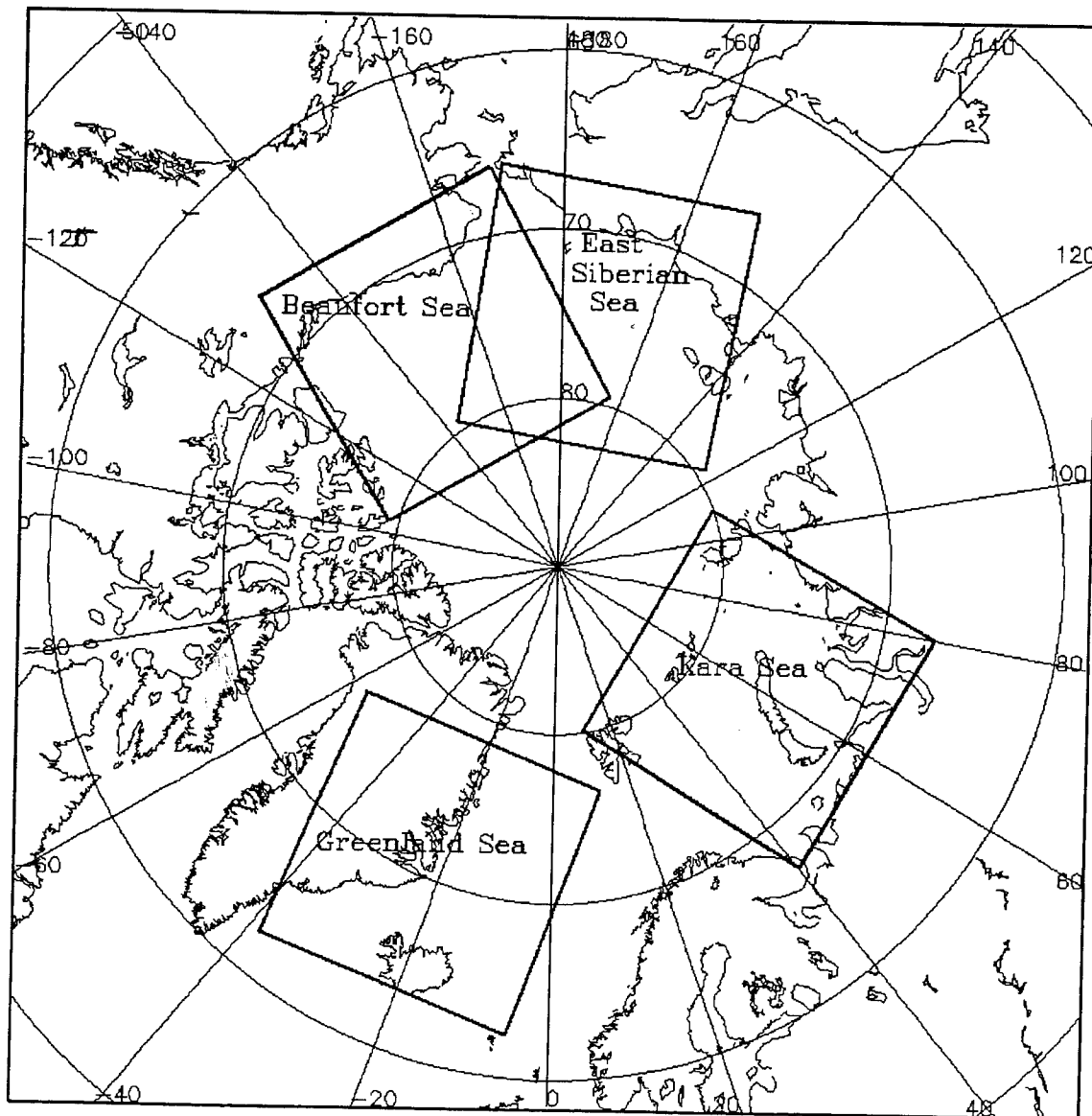


Fig. 1 — Map of regional projections used to compare multisensor combination techniques

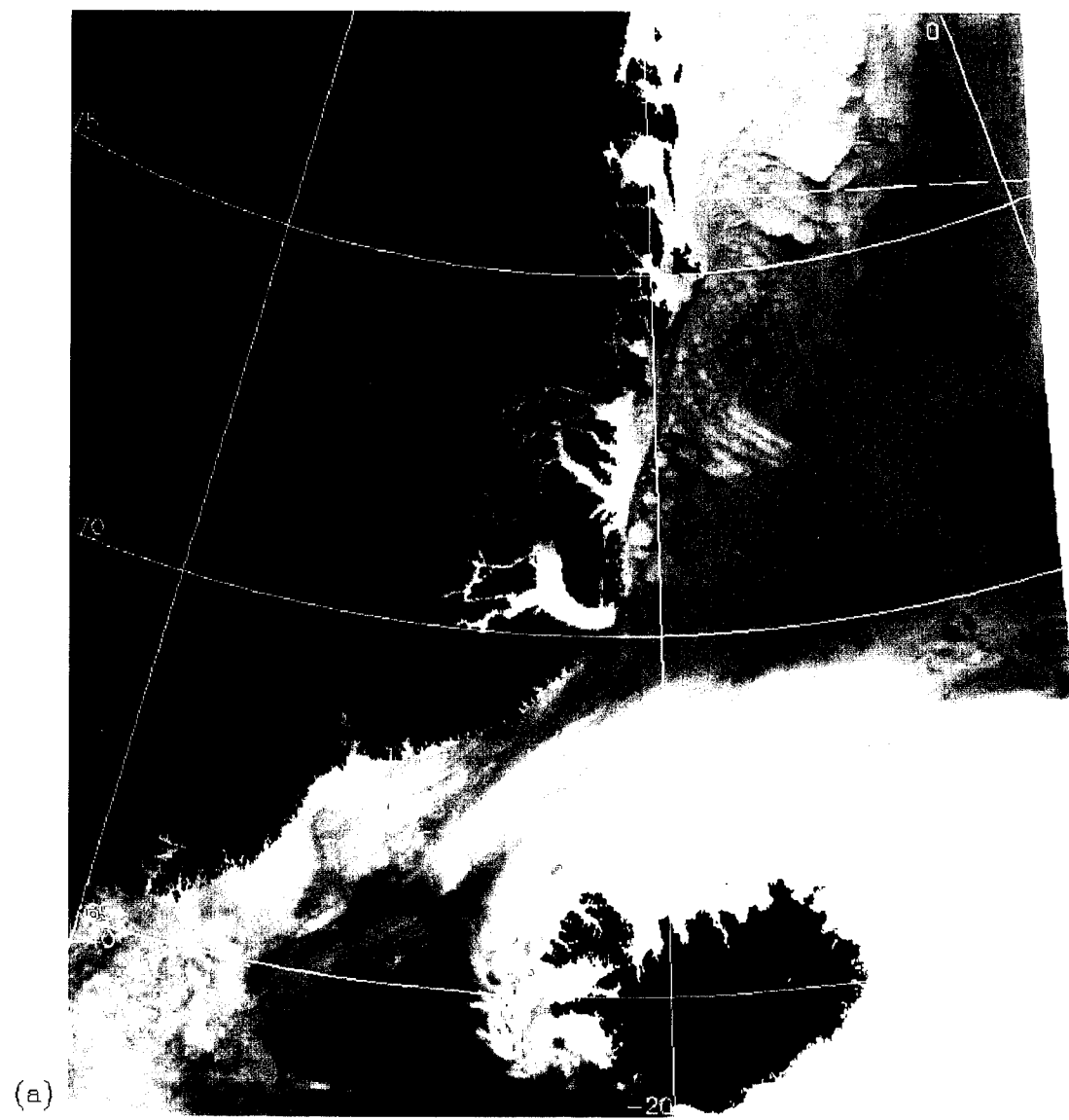


Fig. 2 — The 22 Jan 89 Greenland Sea test case, (a) inverted infrared image

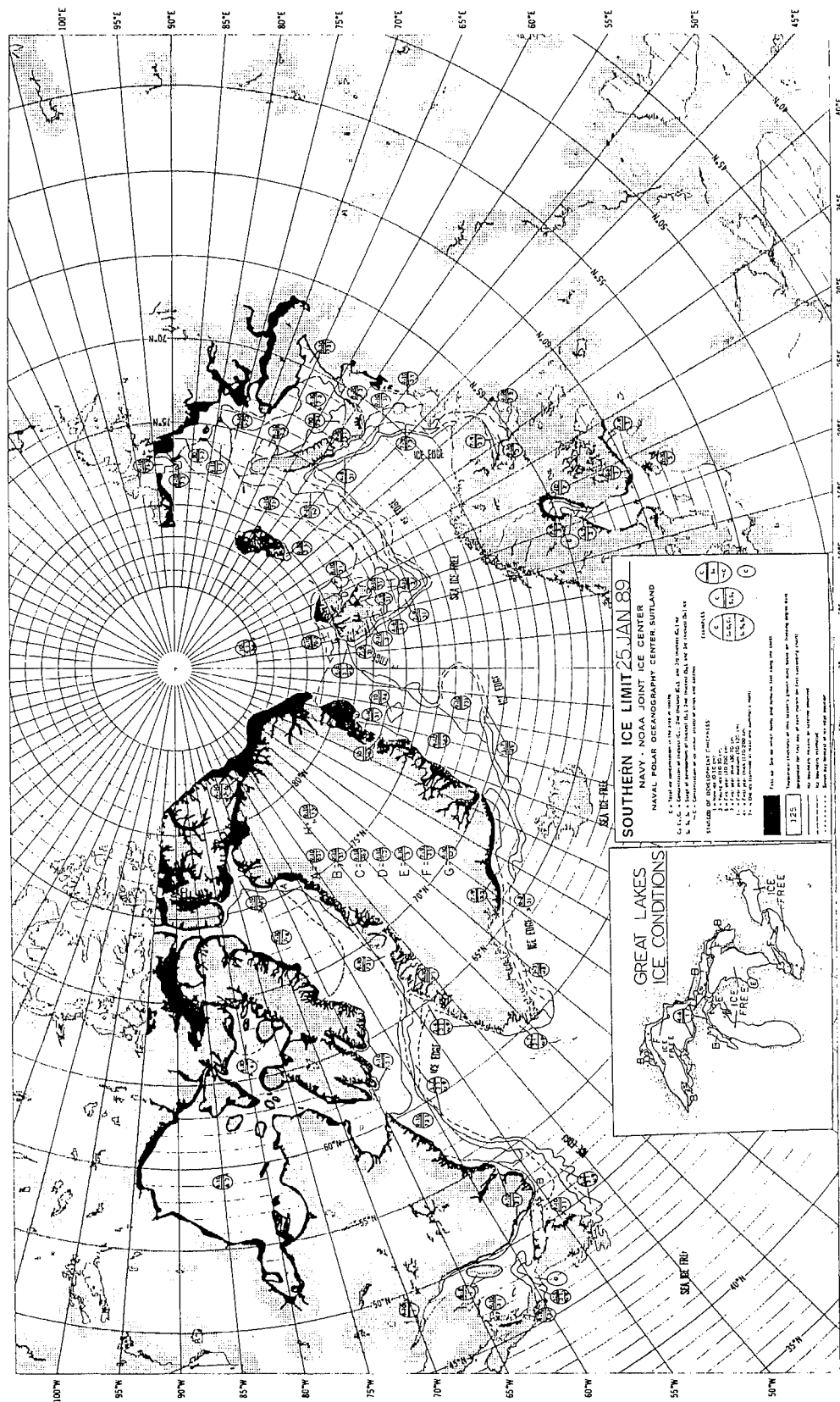


Fig. 2—Continued (b) NAVICECEN ice chart for 25 Jan 89

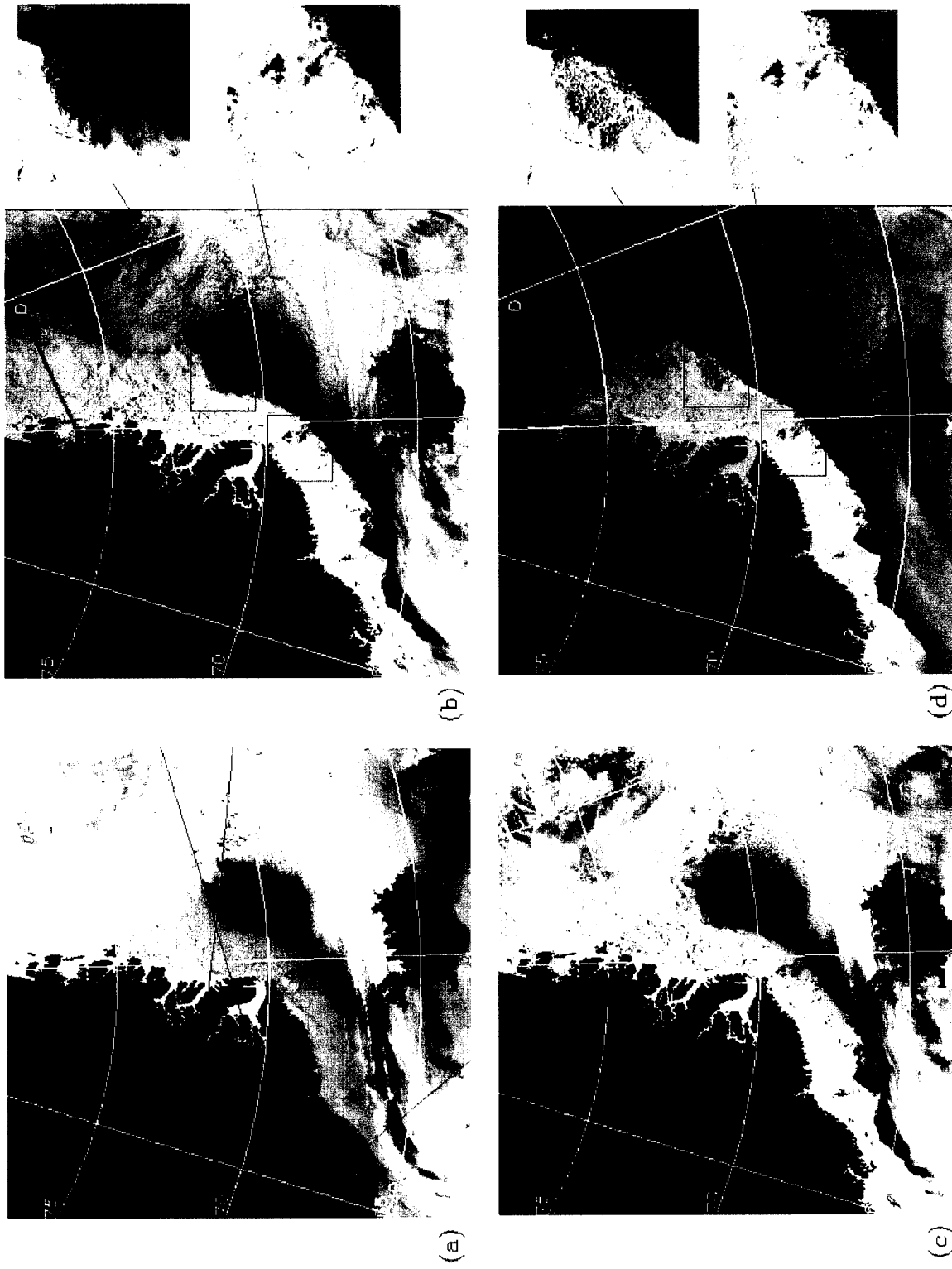


Fig. 3—Comparison of the difference and contrast products to visible and infrared data for the 20 Apr 89 Greenland Sea test case, (a) inverted infrared data overlain with Geosat altimeter tracks, (b) visible data, (c) contrast product, and (d) difference product. High resolution subareas show improvement. B, D, and E represent altimeter track locations.

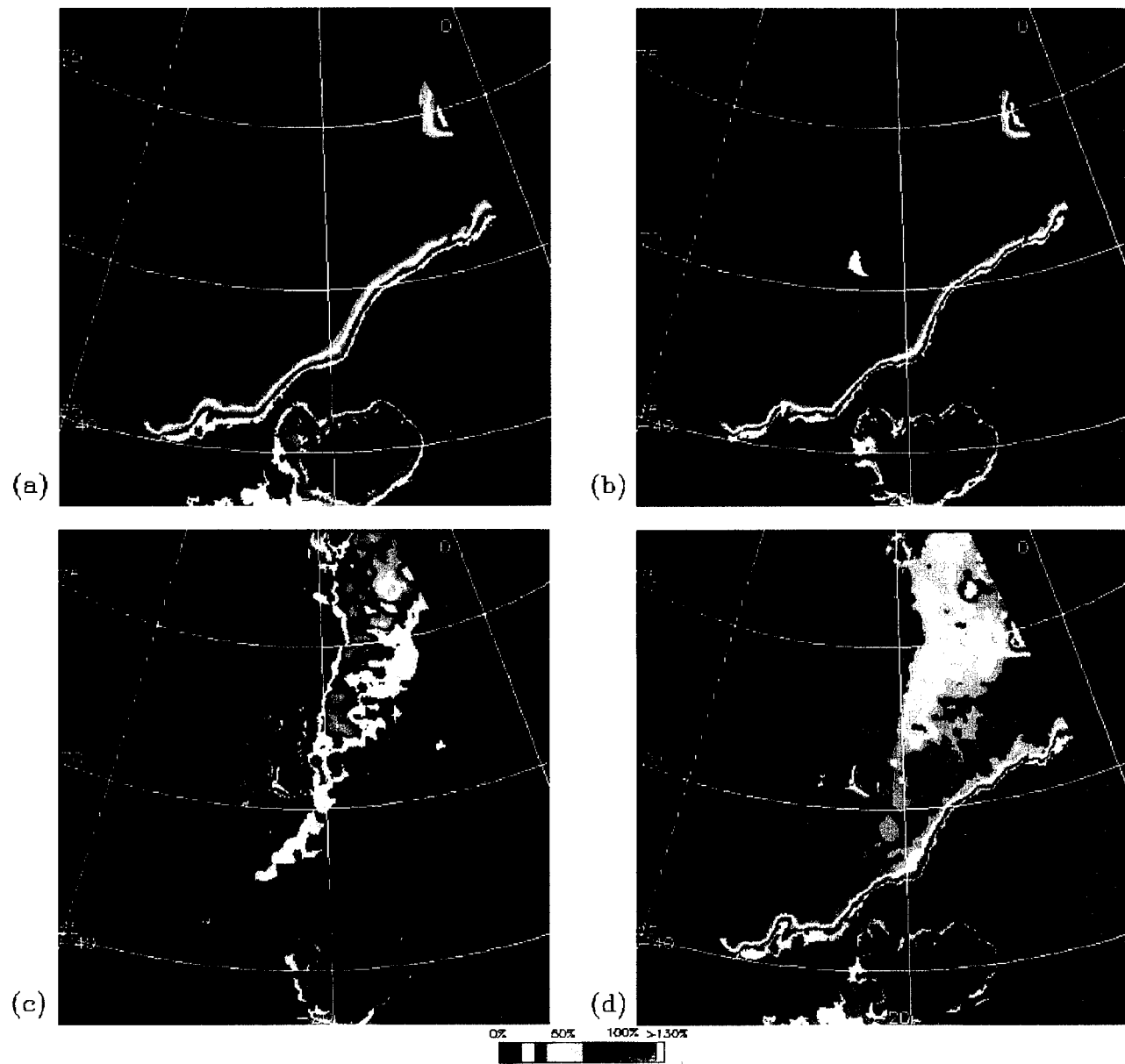


Fig. 4 — SSM/I data for the 22 Jan 89 Greenland Sea test case, (a) total ice concentration, NASA algorithm, (b) total ice concentration, Navy algorithm, (c) multiyear ice concentration, NASA algorithm, (d) first-year ice concentration, NASA algorithm

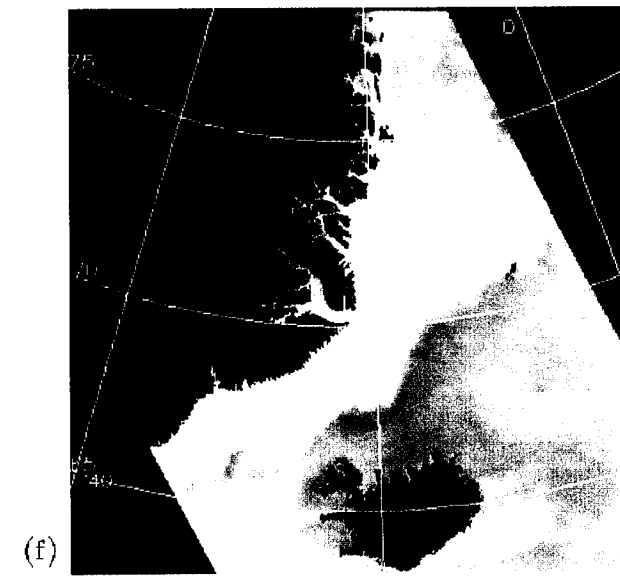
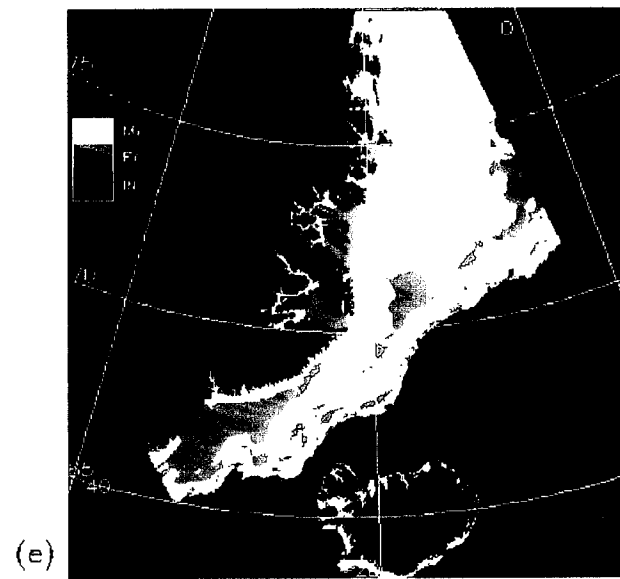


Fig. 4 — Continued (e) ice type predominance, Navy algorithm and (f) 85 GHz H-pol brightness temperatures

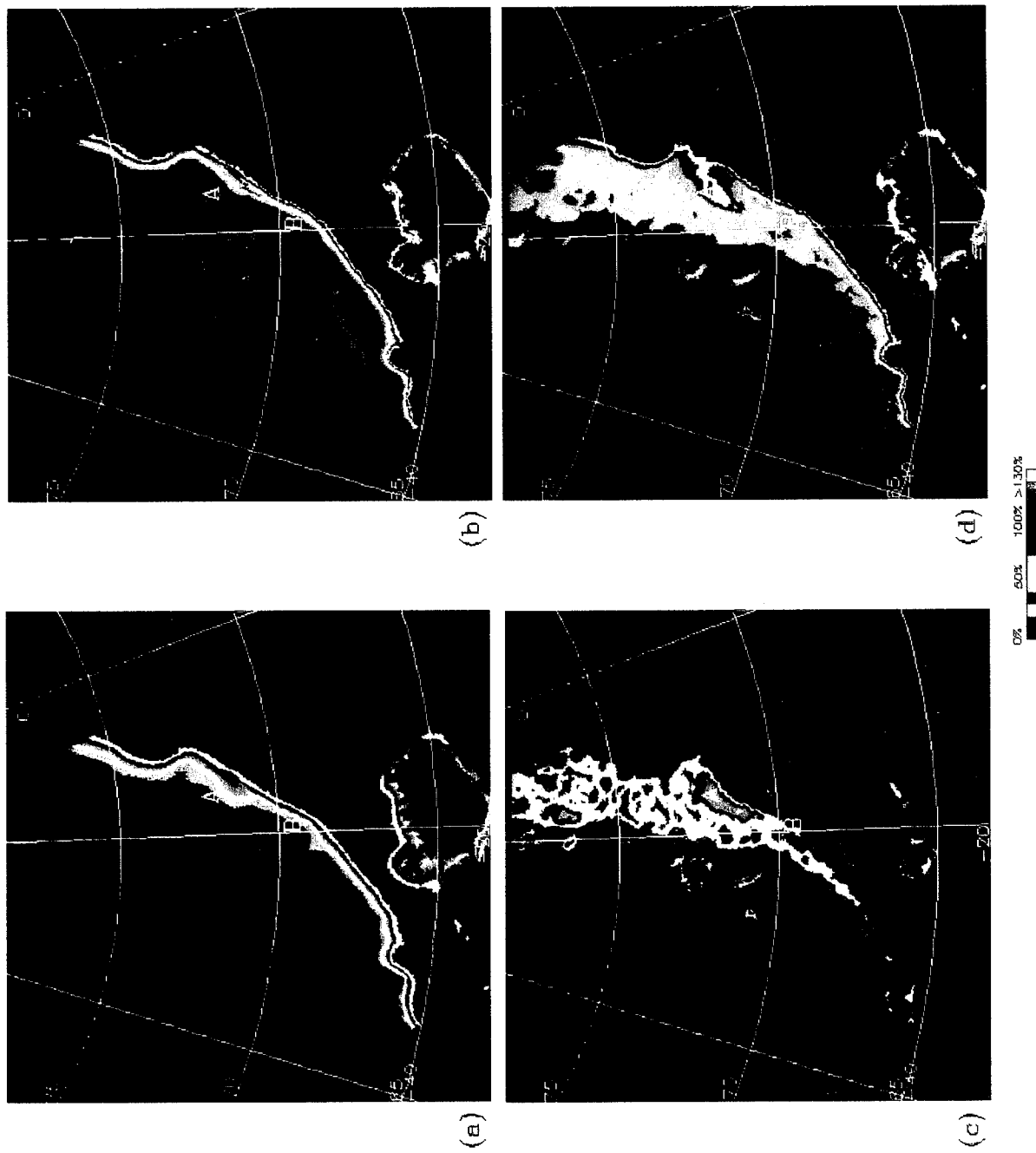


Fig. 5 — SSM/I data for the 20 Apr 89 Greenland Sea test case, (a) total ice concentration, NASA algorithm, (b) total ice concentration, Navy algorithm, (c) multiyear ice concentration, NASA algorithm, (d) first-year ice concentration, NASA algorithm

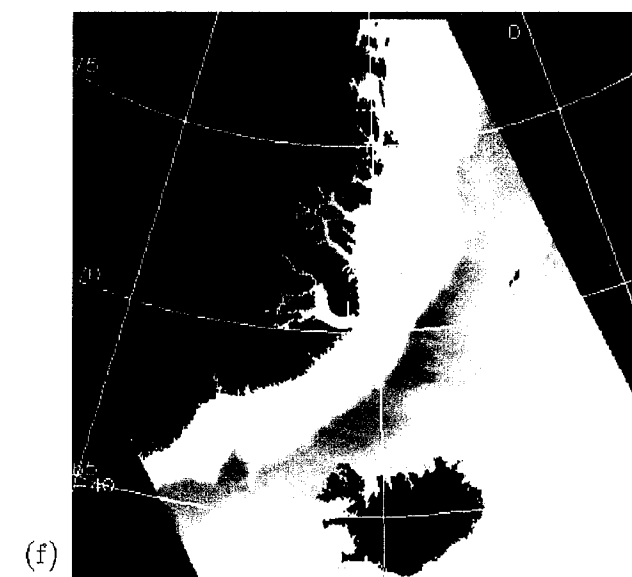
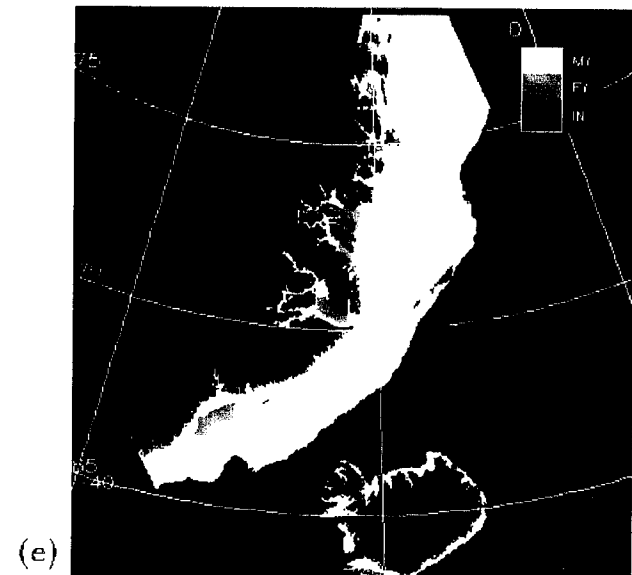


Fig. 5 — Continued (e) ice type predominance, Navy algorithm and (f) 85 GHz H-pol brightness temperatures

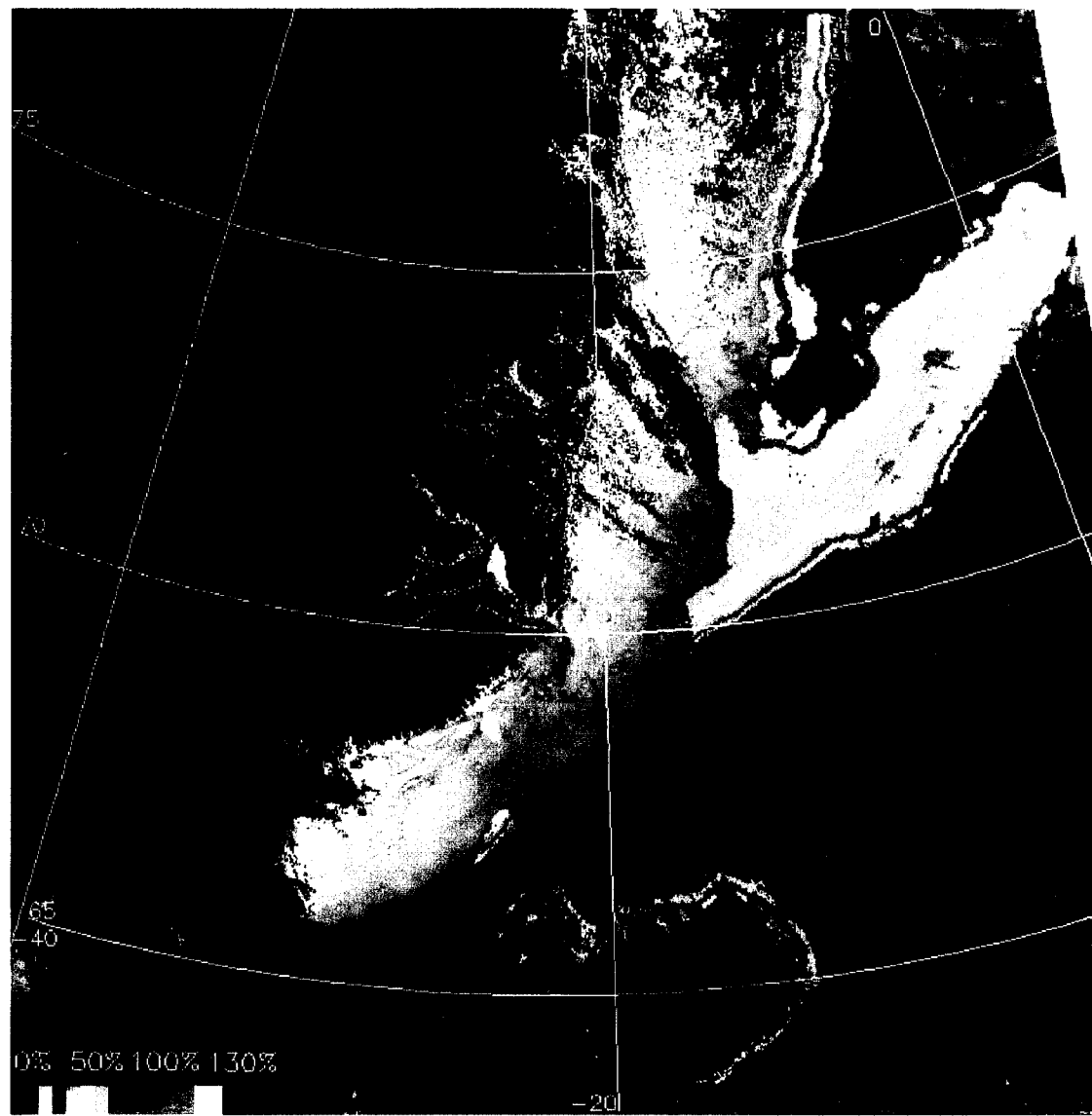


Fig. 6 — AVHRR/Navy total ice concentration composite for the 15 Mar 89 Greenland Sea test case

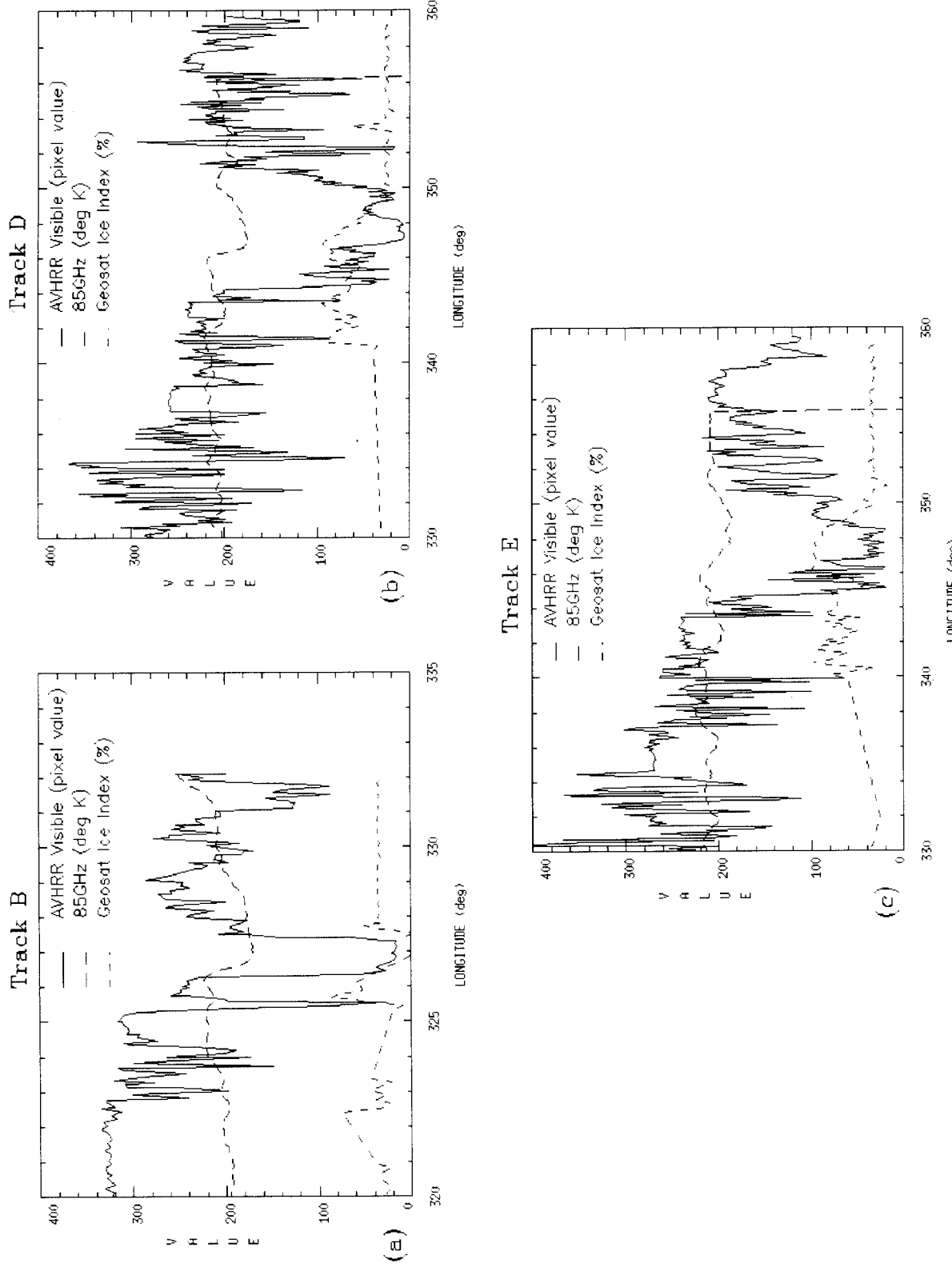


Fig. 7 — Comparisons of AVHRR visible, 85 GHz, and Geosat ice index estimates for the 20 Apr 89 Greenland Sea test case, (a) data from track B, (b) data from track D, and (c) data from track E

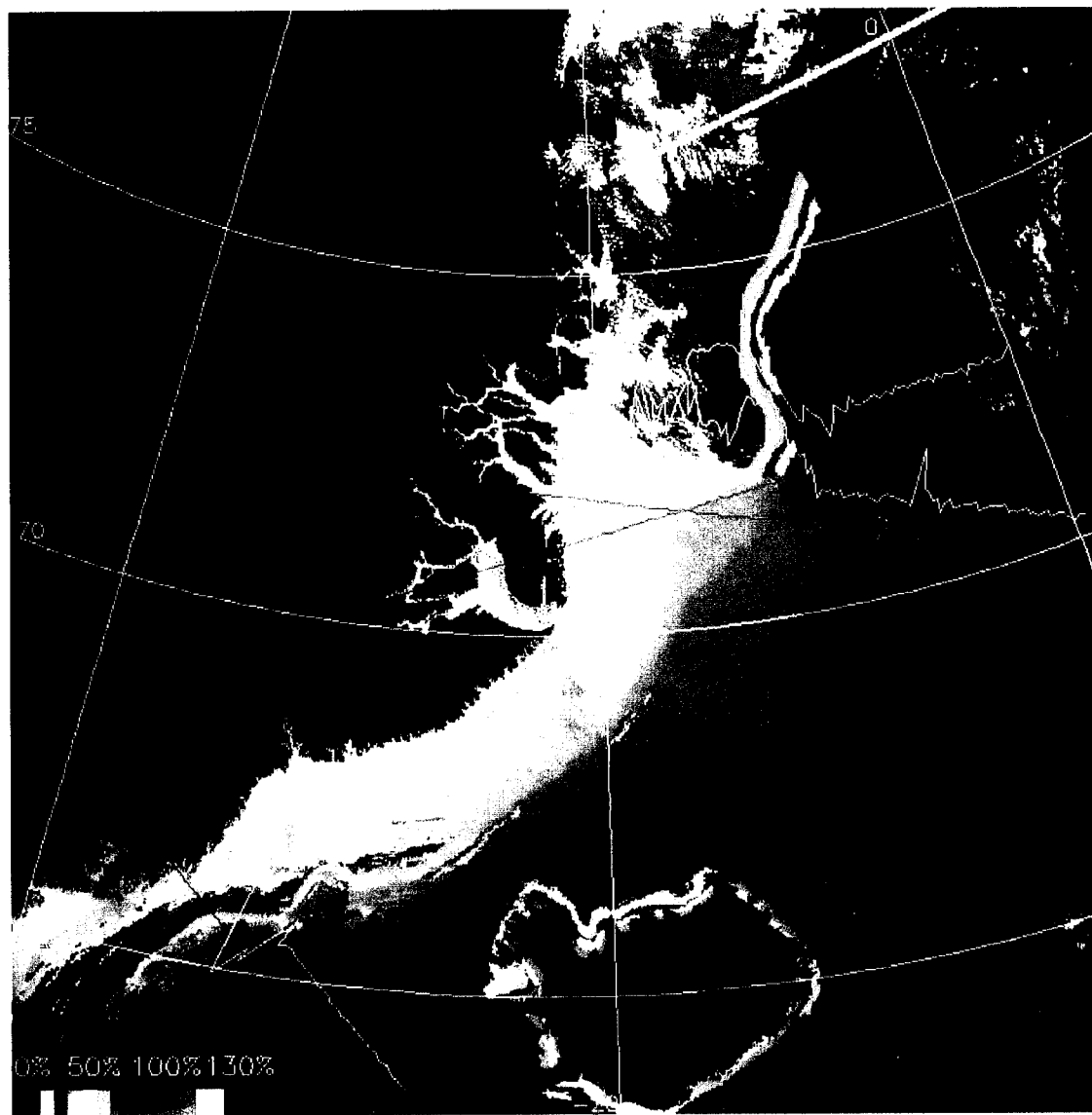


Fig. 8 — AVHRR/Navy total ice concentration composite for the 20 Apr 89 Greenland Sea test case overlain with the Geosat ice index estimates. The value of the ice index estimates is given in Fig. 7. The red lines represent the altimeter track location and the yellow lines indicate ice index values retrieved along each respective track.

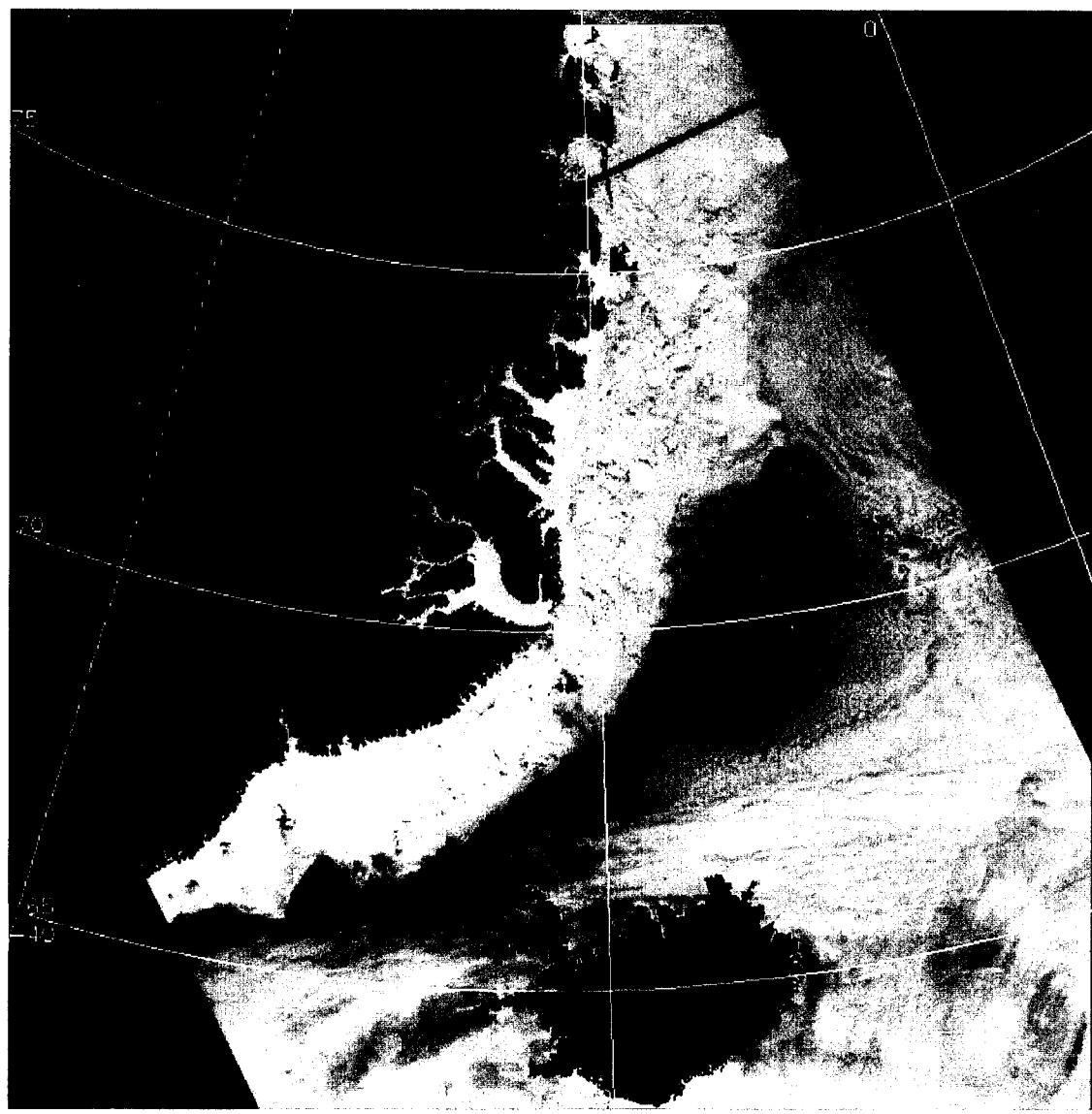


Fig. 9 — A red/green/blue composite of 85 GHz SSM/I (red), AVHRR visible (green), and AVHRR infrared (blue) data for the 20 Apr 89 Greenland Sea test case

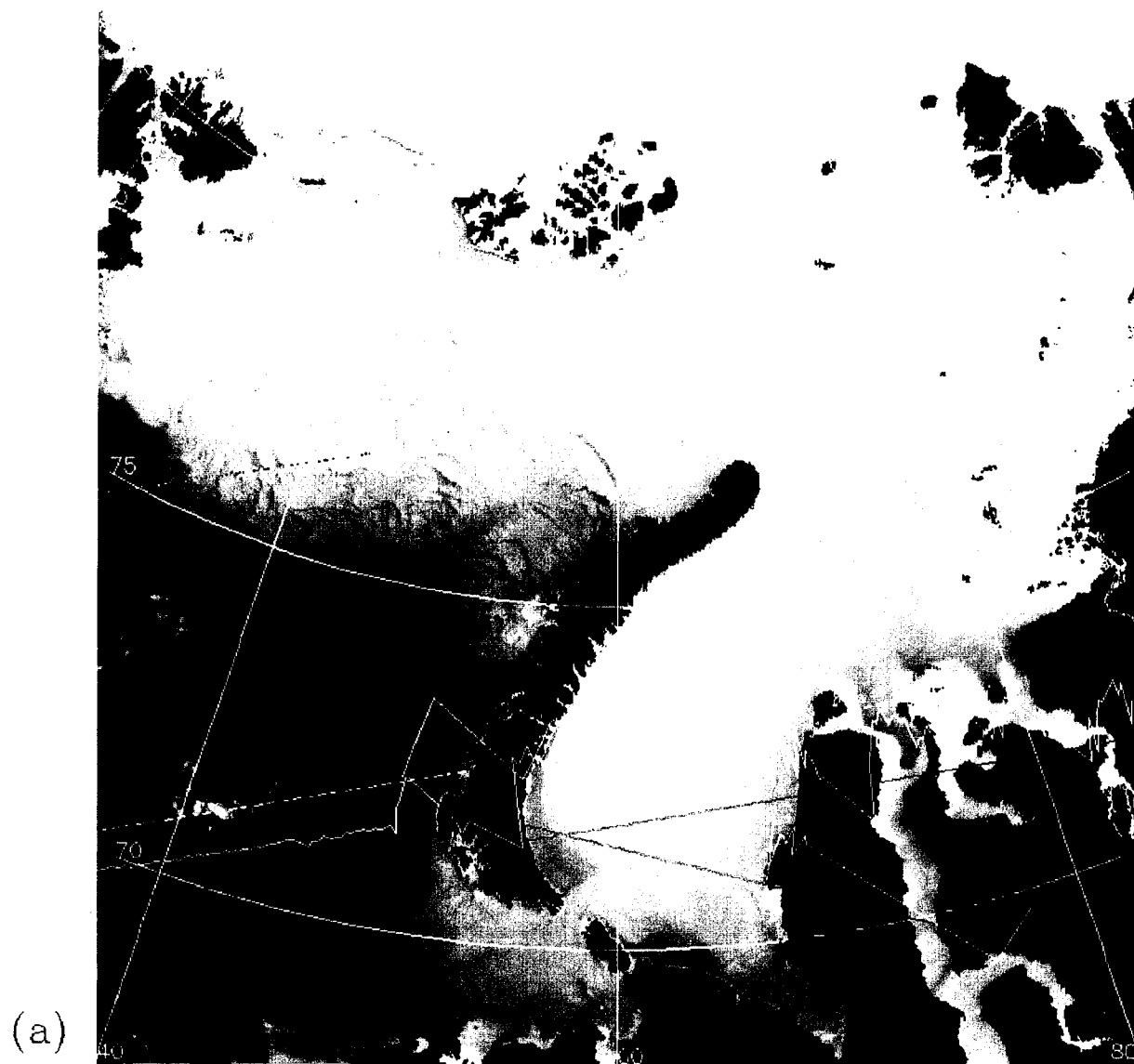


Fig. 10 — The 25 Feb 89 Kara Sea test case, (a) inverted infrared image overlain with Geosat altimeter tracks and Geosat ice index estimates. The value of the ice index estimates is given in Fig. 13.

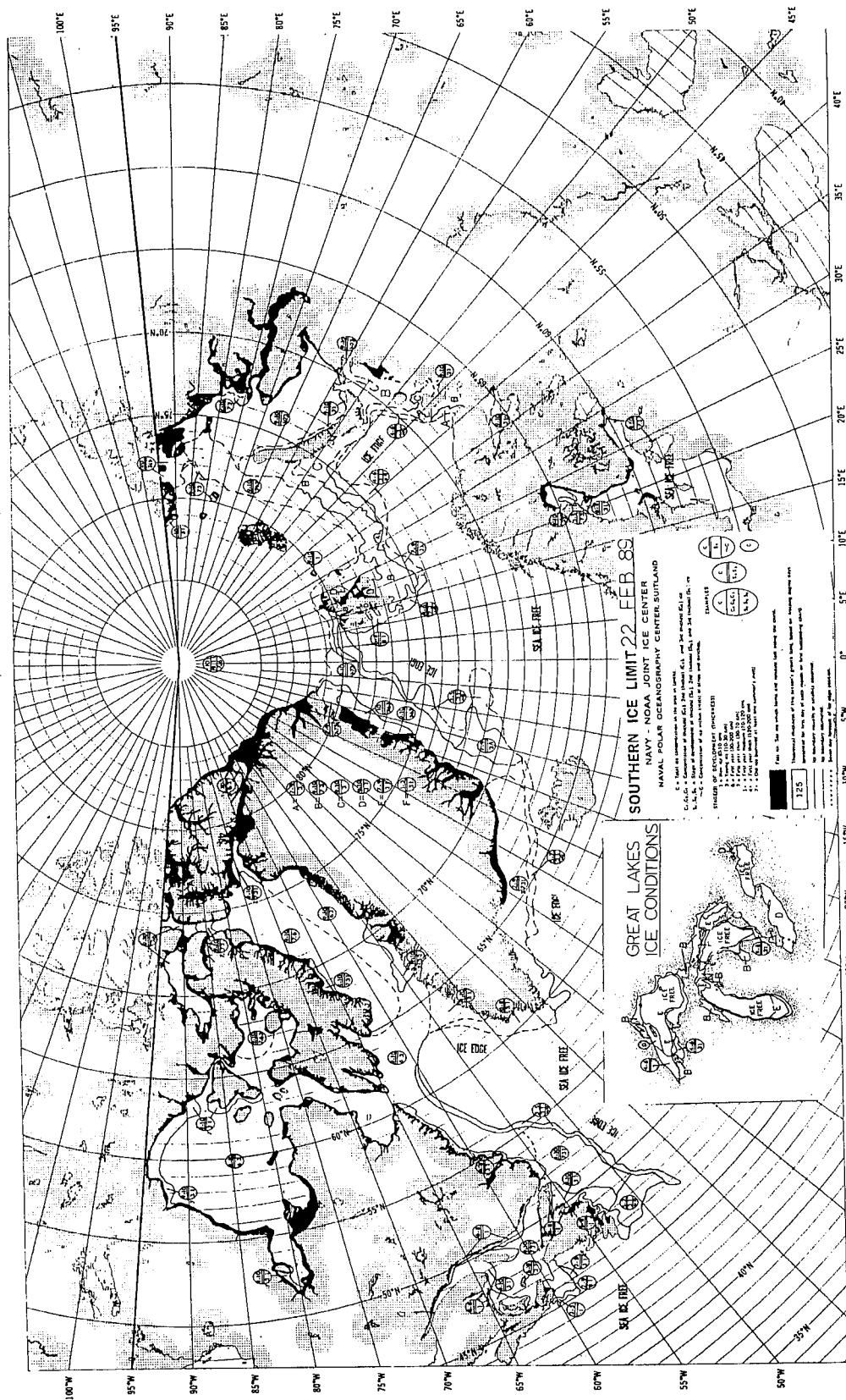


Fig. 10 — Continued (b) NAVICECEN ice chart for 22 Feb 89

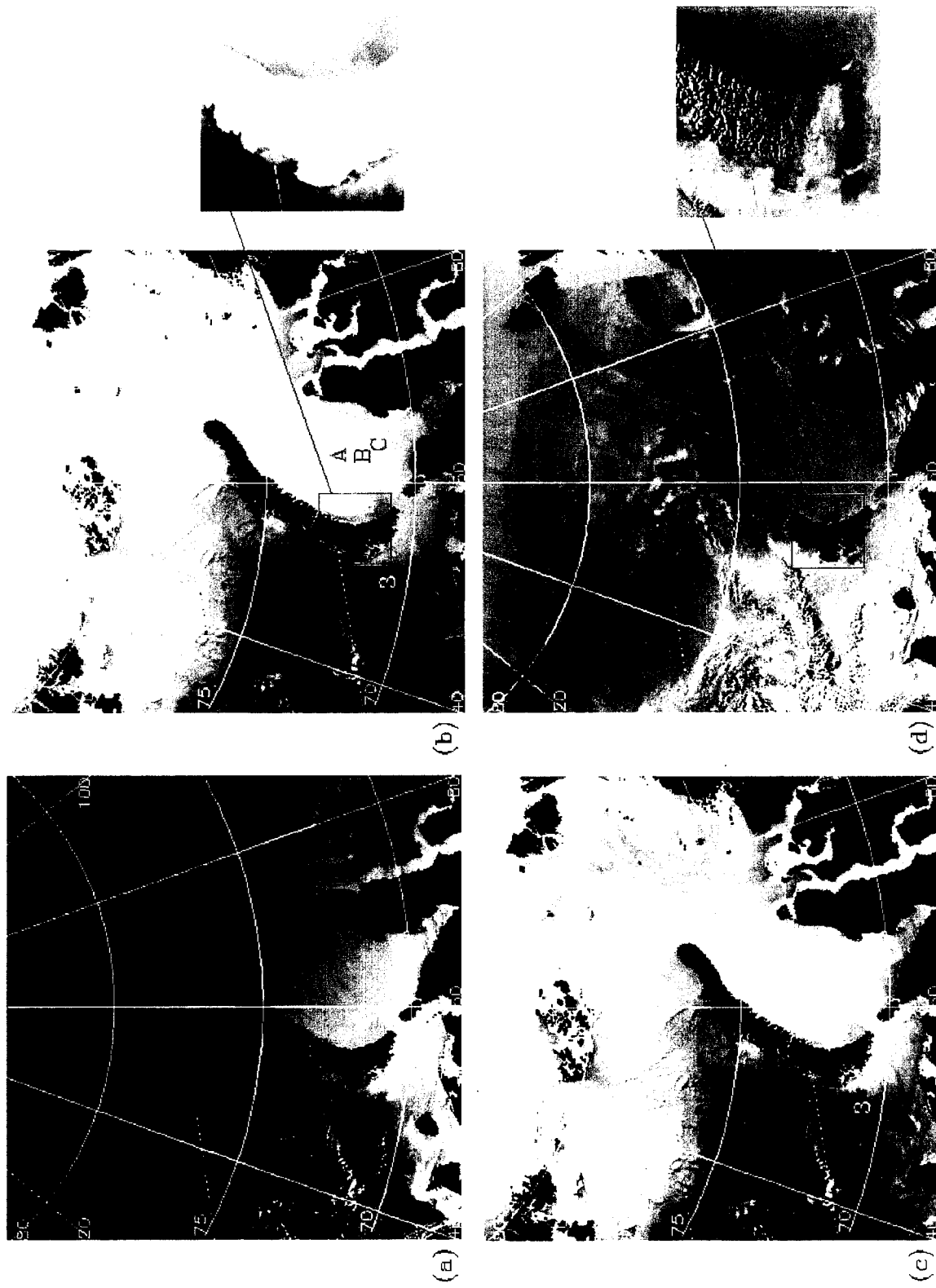


Fig. 11 — Comparison of the difference and contrast products to visible and infrared data for the 25 Feb 89 Kara Sea test case, (a) visible data, (b) inverted infrared data, (c) contrast product, and (d) difference product. High resolution subareas show improvement. Areas 1, 2, and 3 were used in the calculations of coefficient of variation listed in Table 3. Areas A, B, and C correspond to SSM/I data in Fig. 12.

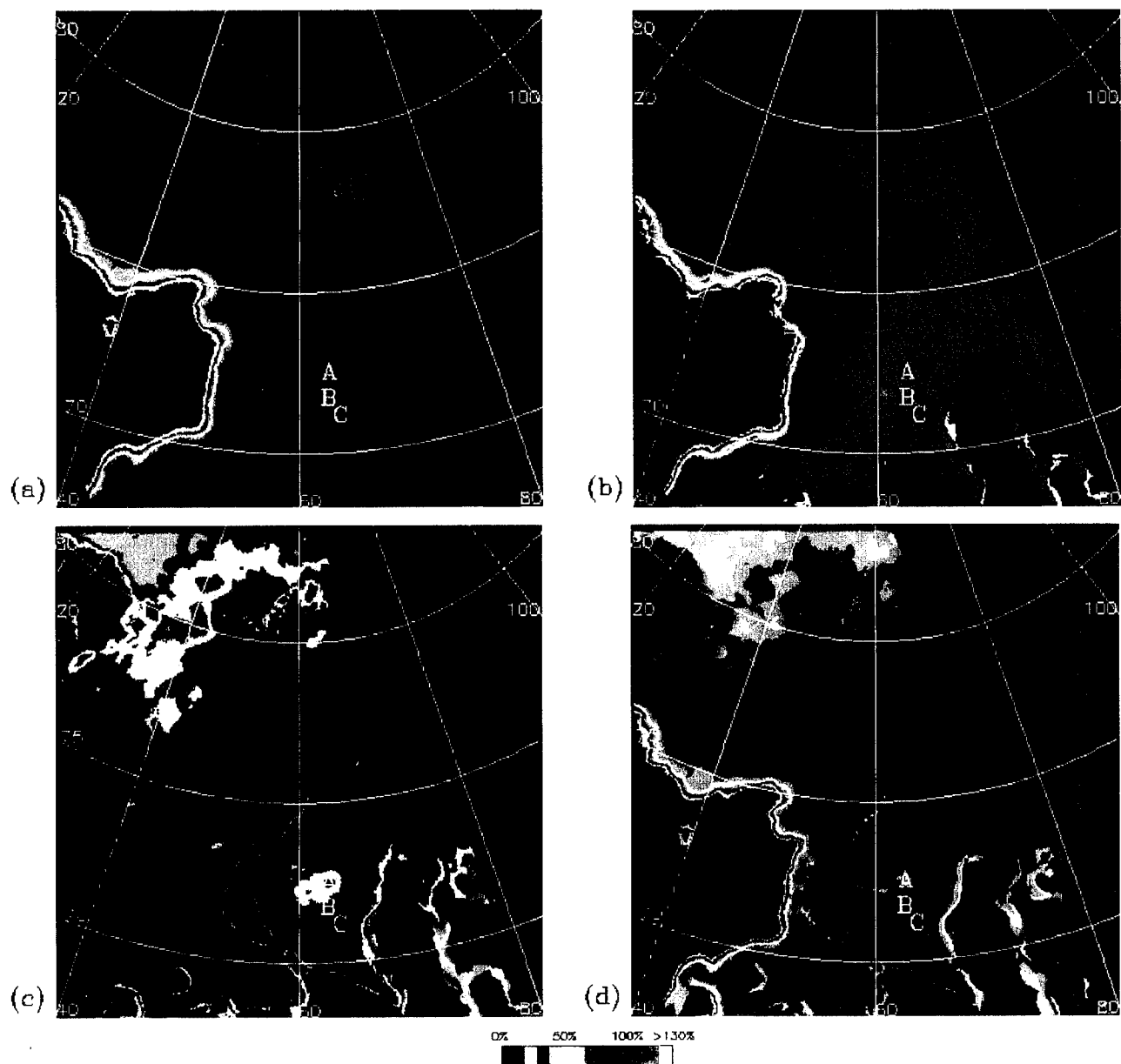


Fig. 12—SSM/I data for the 25 Feb 89 Kara Sea test case, (a) total ice concentration, NASA algorithm, (b) total ice concentration, Navy algorithm, (c) multiyear ice concentration, NASA algorithm, (d) first-year ice concentration, NASA algorithm. A, B, and C mark areas used in the analysis of anomalous SSM/I ice concentrations.

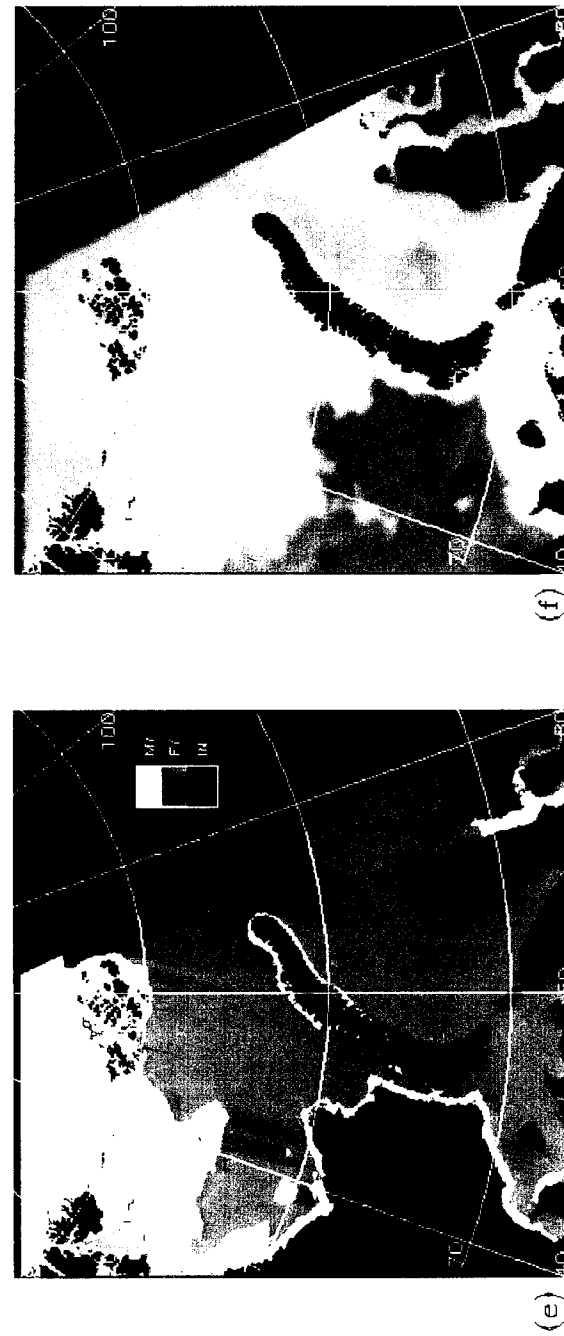


Fig. 12—Continued (e) ice type predominance, Navy algorithm and (f) 85 GHz H-pol brightness temperatures

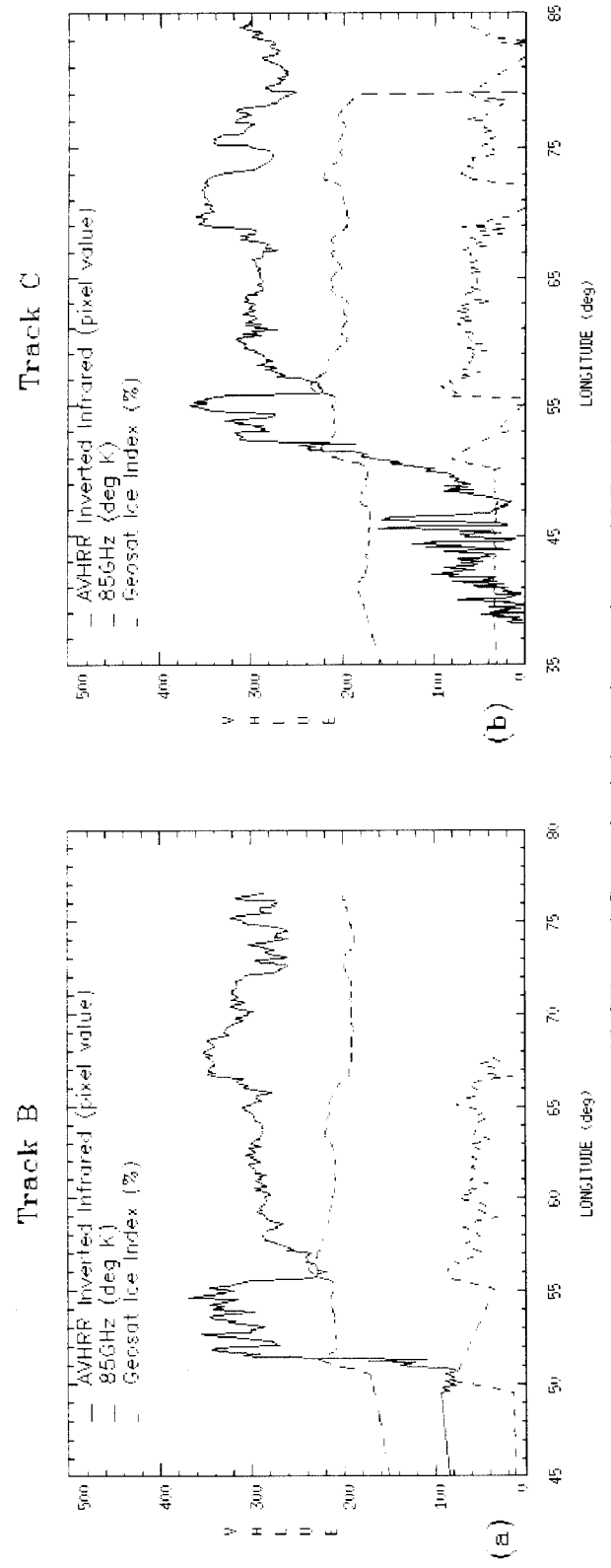


Fig. 13 — Comparisons of AVHRR infrared, 85 GHz, and Geosat ice index estimates for the 25 Feb 89 Kara Sea test case, (a) data from track B and (b) data from track C. Tracks correspond to those appearing on Fig. 10a.

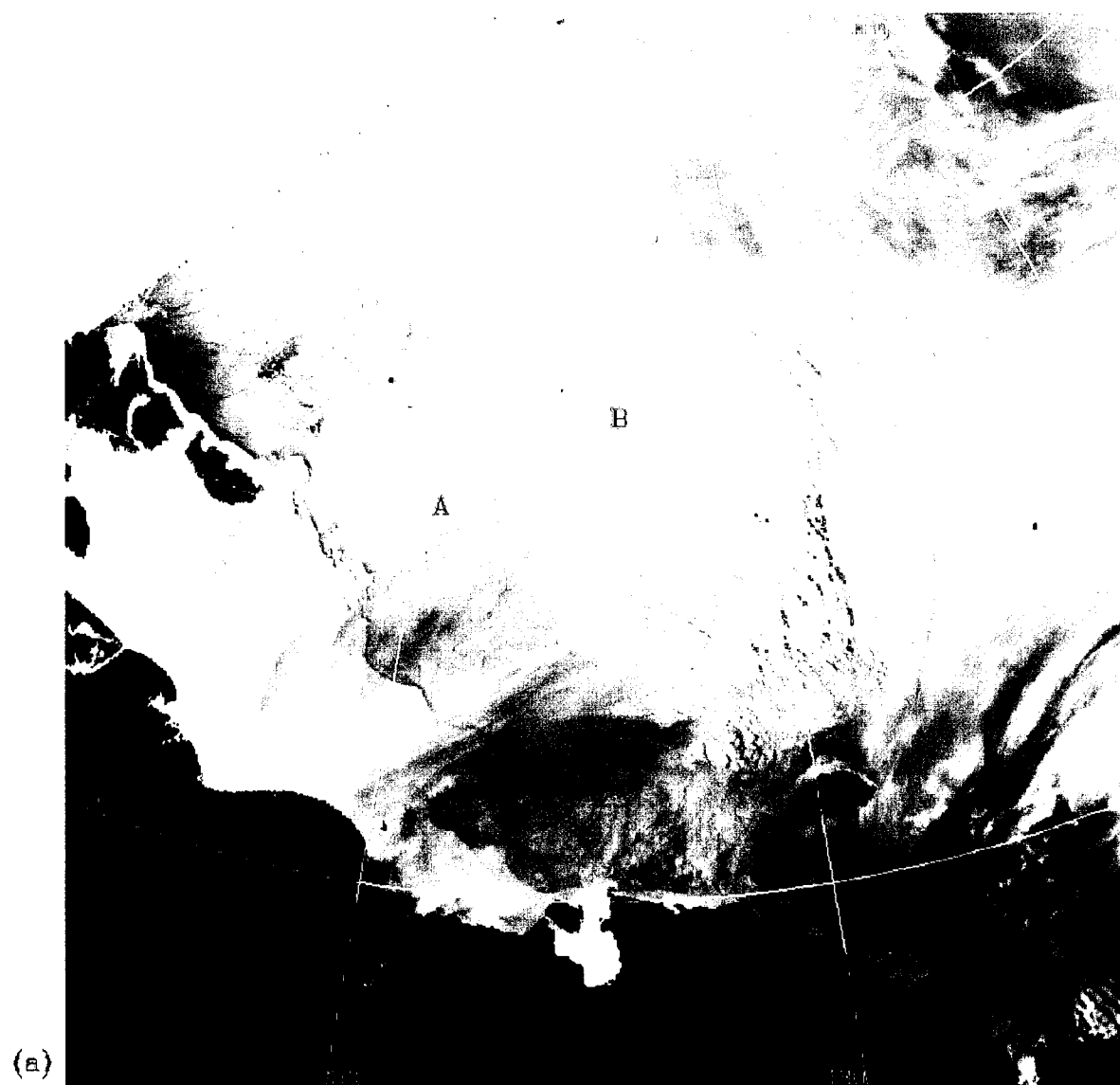


Fig. 14—The 9 Feb 89 East Siberian Sea test case, (a) inverted infrared image. Areas A and B correspond to SSM/I data in Fig. 16.

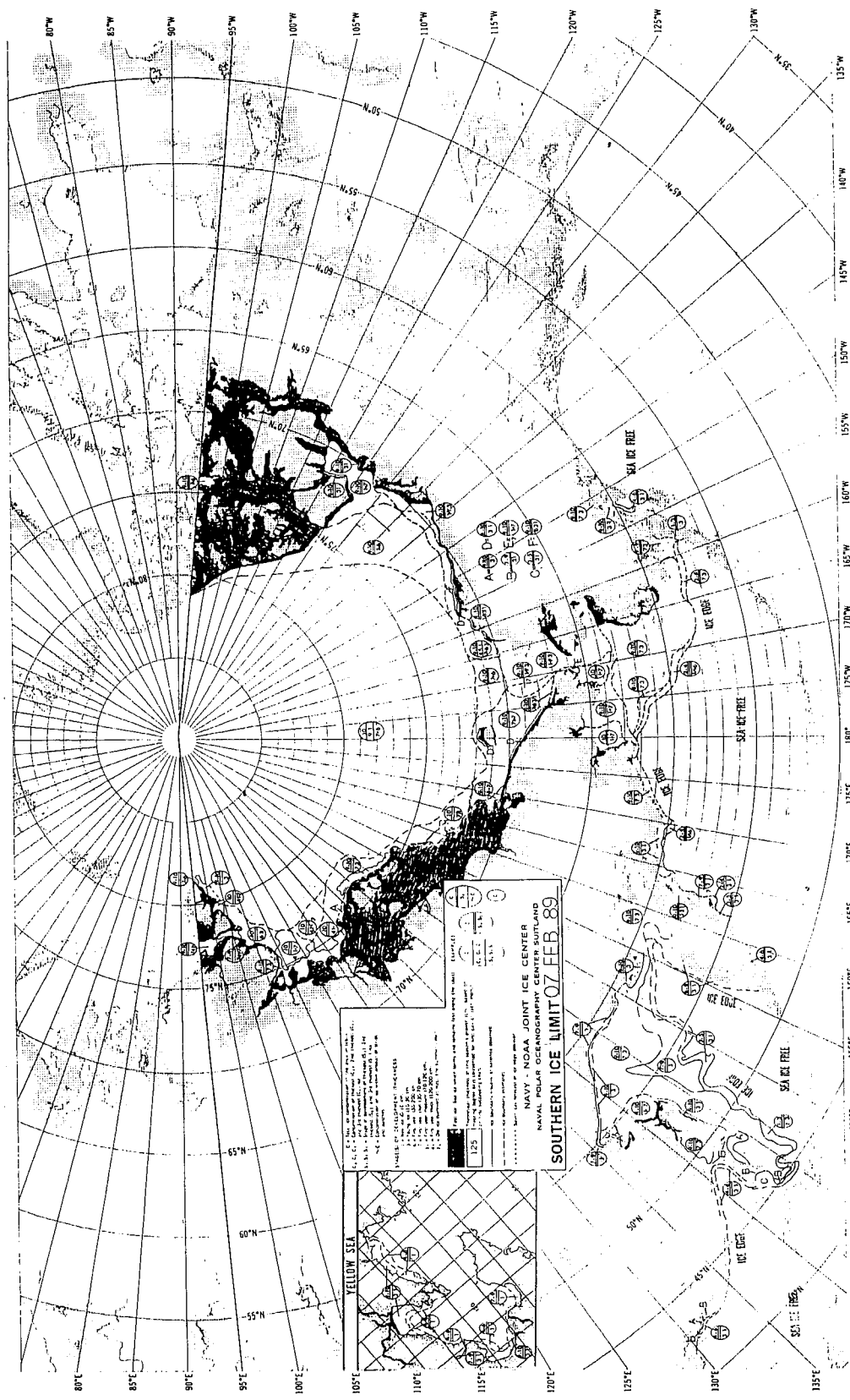


Fig. 14—Continued (b) NAVICECEN ice chart for 7 Feb 89

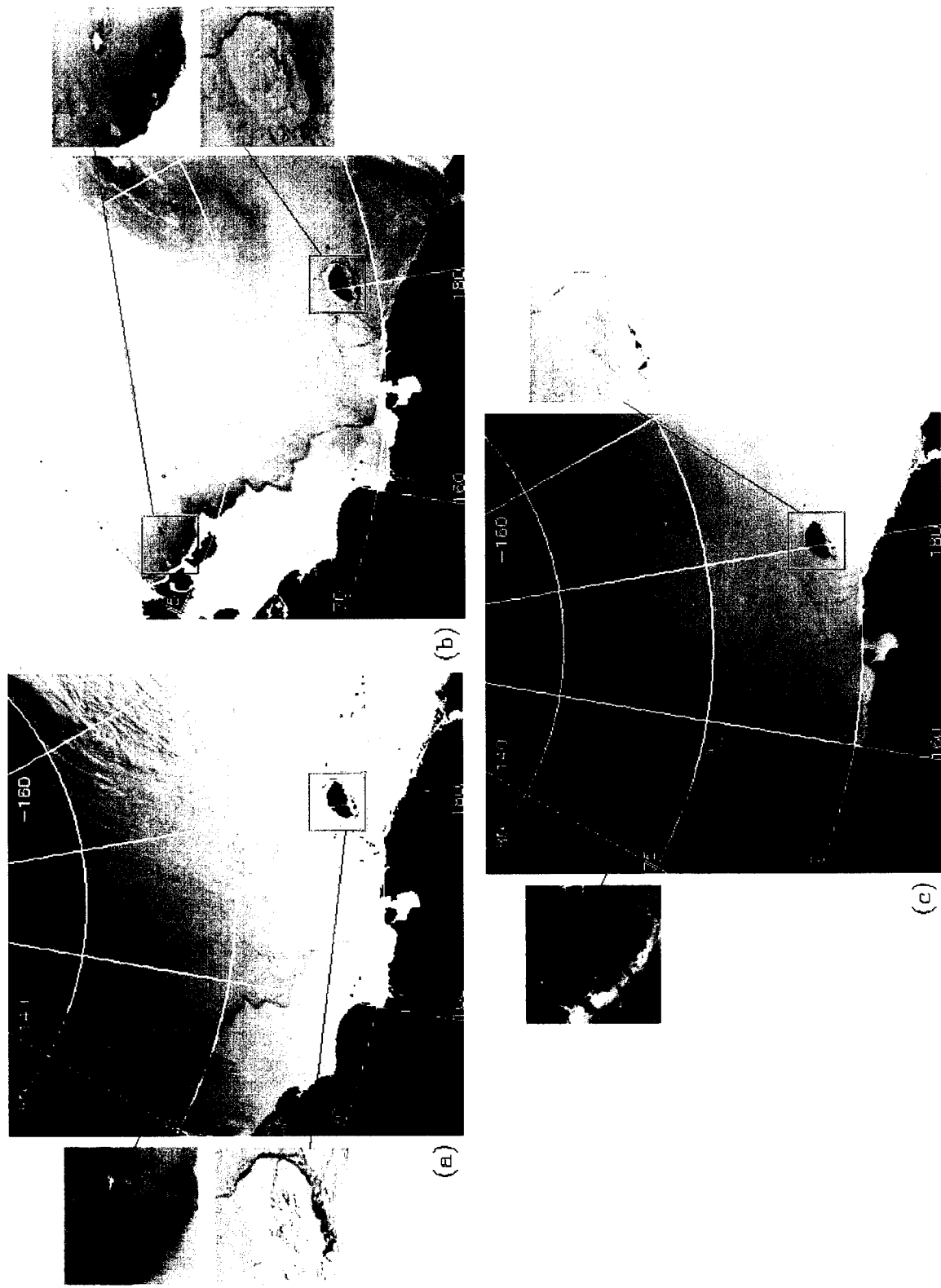


Fig. 15—Comparison of the difference product to visible and infrared data for the 11 Apr 89 East Siberian Sea test case, (a) visible data, (b) inverted infrared data, and (c) difference product. High resolution subareas show improvement.

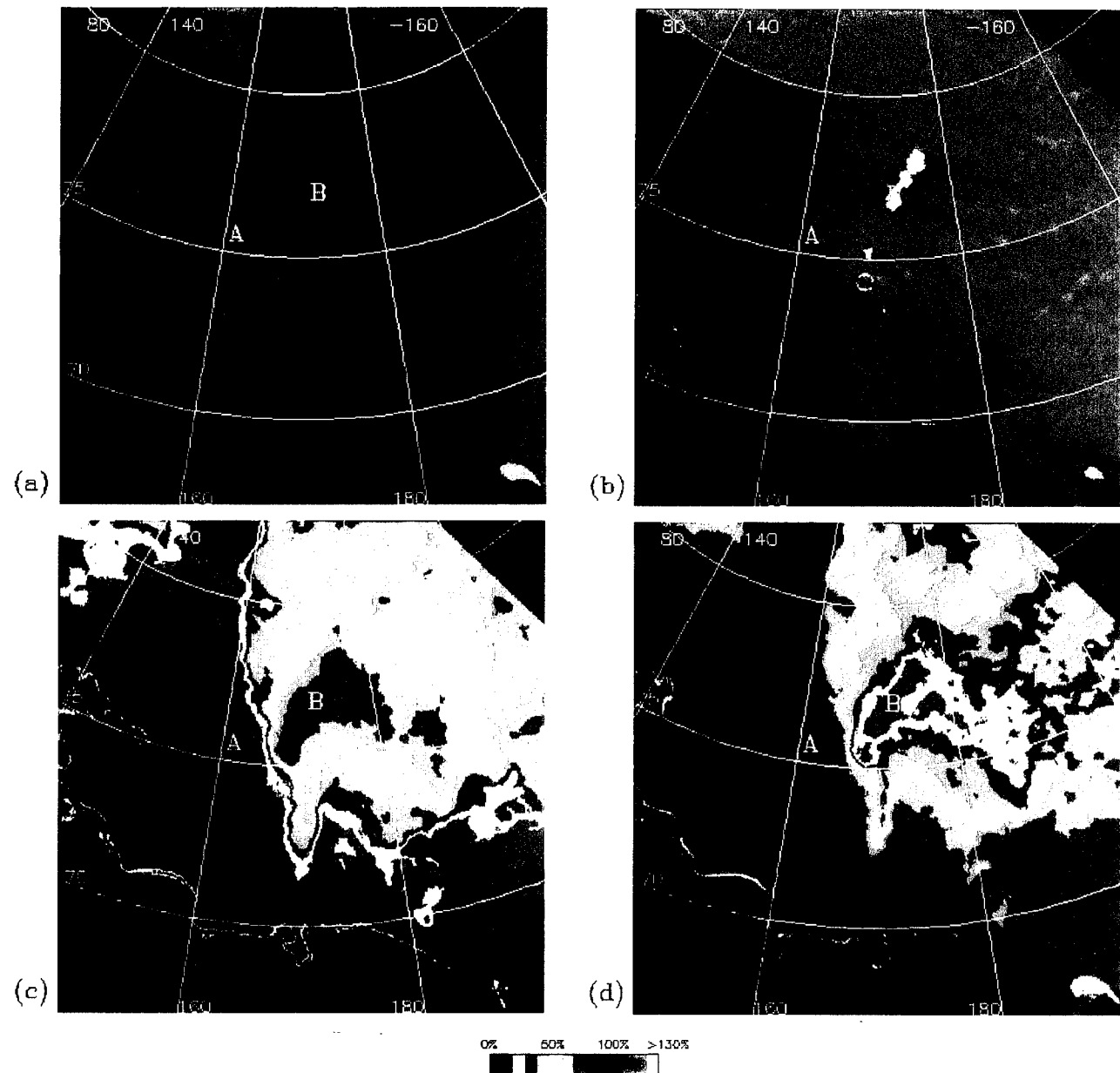


Fig. 16—SSM/I data for the 9 Feb 89 East Siberian Sea test case, (a) total ice concentration, NASA algorithm, (b) total ice concentration, Navy algorithm, (c) multiyear ice concentration, NASA algorithm, (d) first-year ice concentration, NASA algorithm

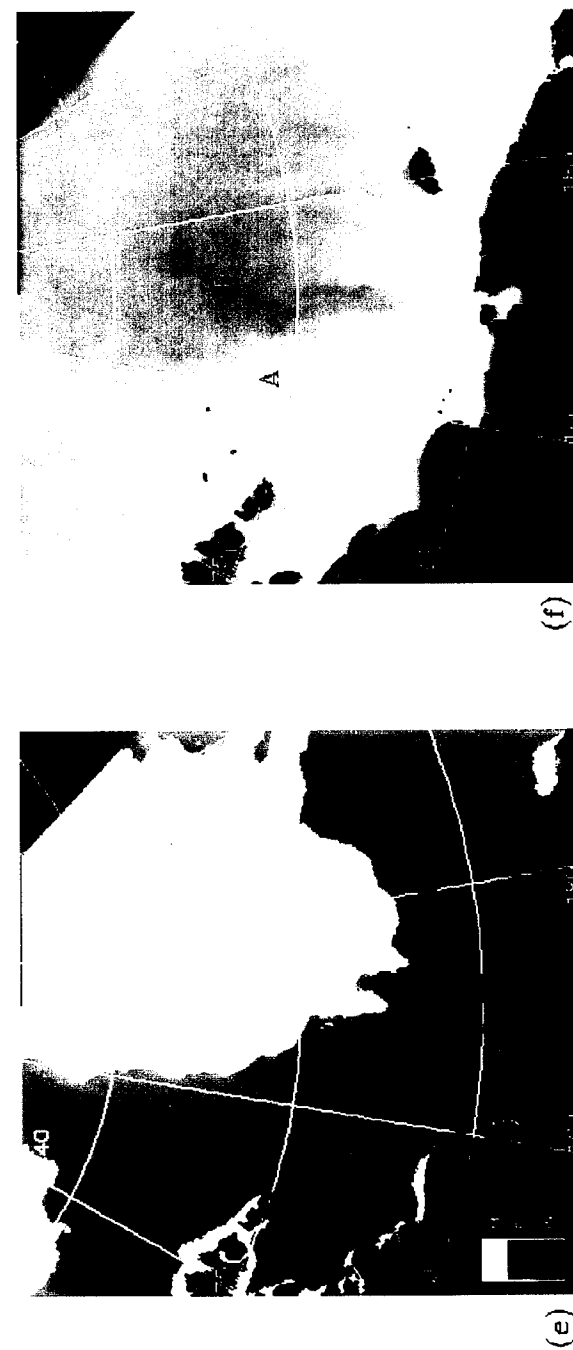


Fig. 16—Continued (e) ice type predominance, Navy algorithm and (f) 85 GHz H-pol brightness temperatures. A and B mark areas used for analysis on either side of the multiyear/first-year boundary.

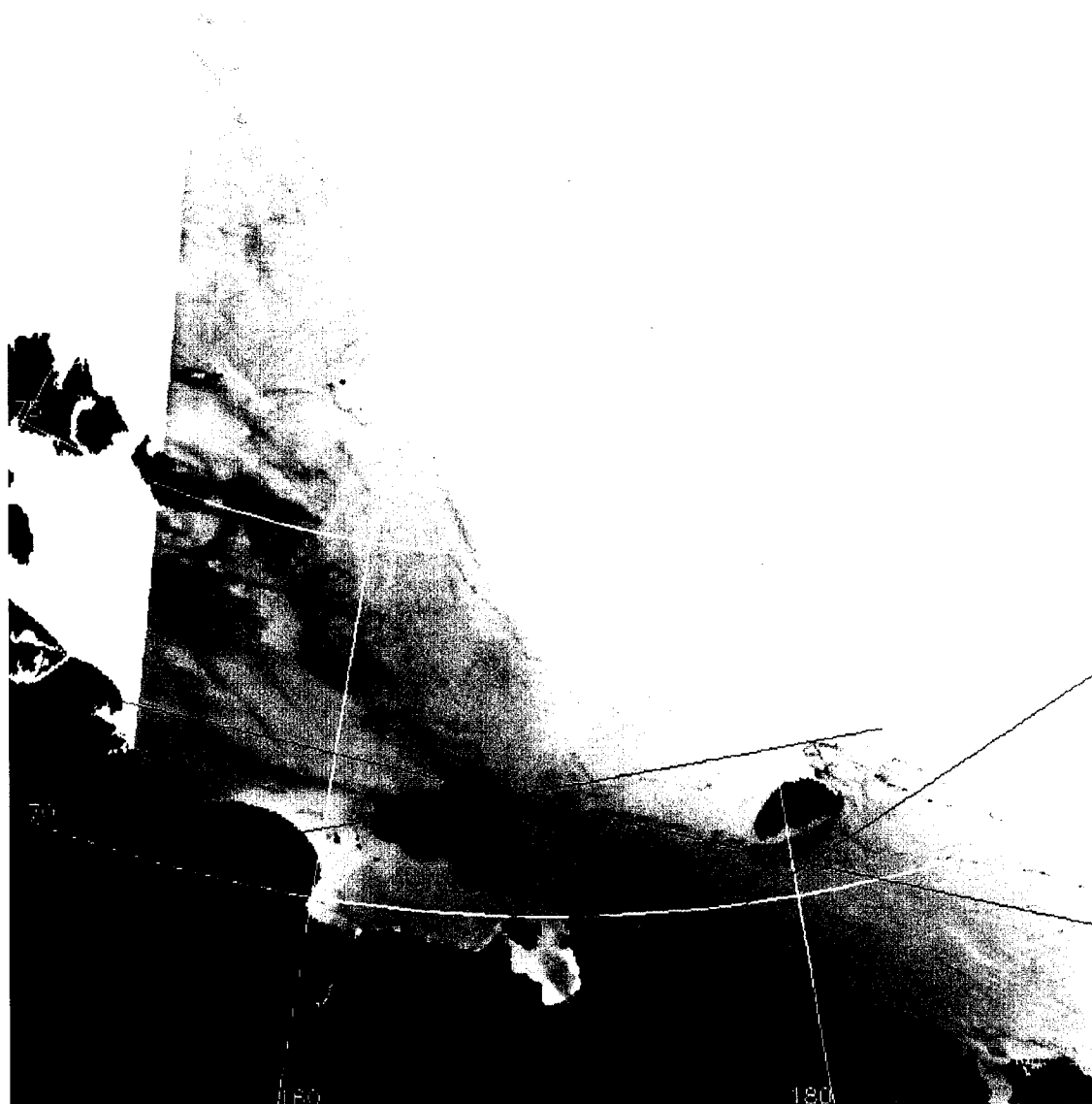


Fig. 17—AVHRR inverted infrared image from the 25 Jan 89 East Siberian Sea test case overlain with Geosat altimeter tracks

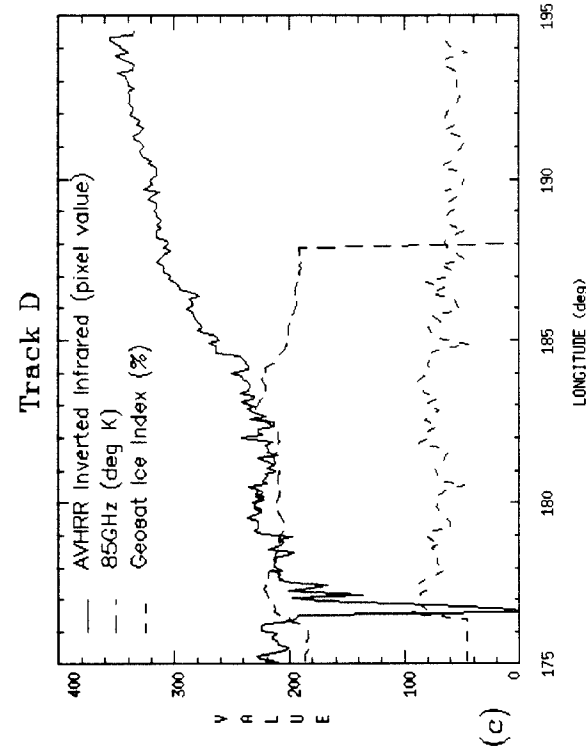
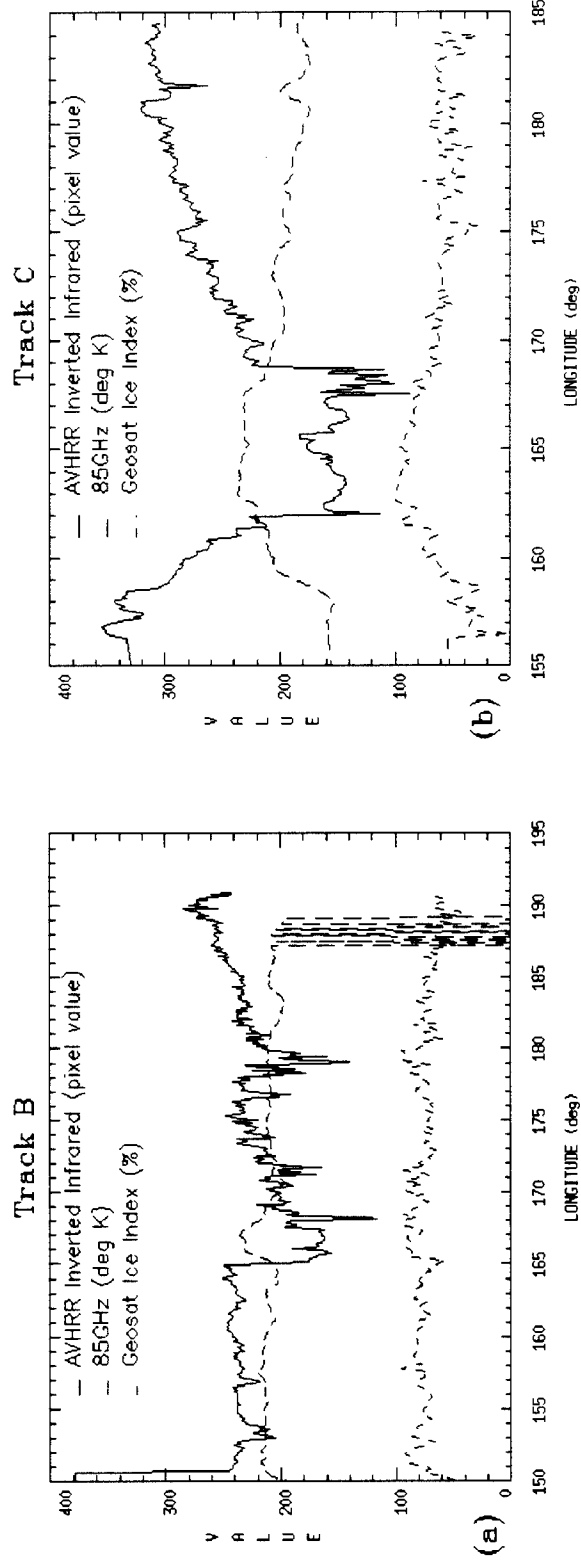


Fig. 18—Comparisons of AVHRR infrared, 85 GHz, and Geosat ice index estimates for the 25 Jan 89 East Siberian Sea test case, (a) data from track B, (b) data from track C, and (c) data from track D



Fig. 19—The 8 Apr 89 Beaufort Sea test case, (a) inverted infrared image

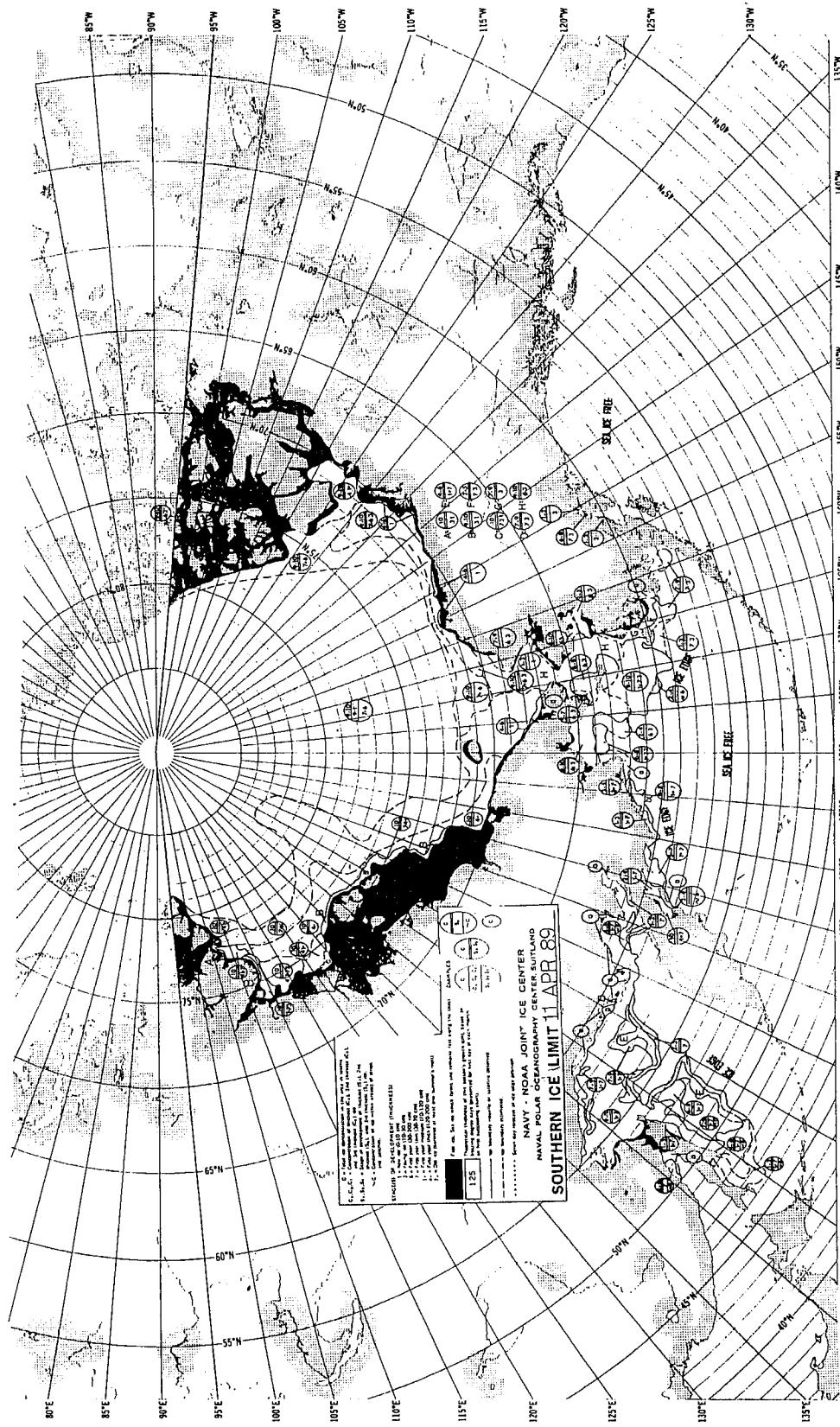


Fig. 19 — Continued (b) NAVICECEN ice chart for 11 Apr 89

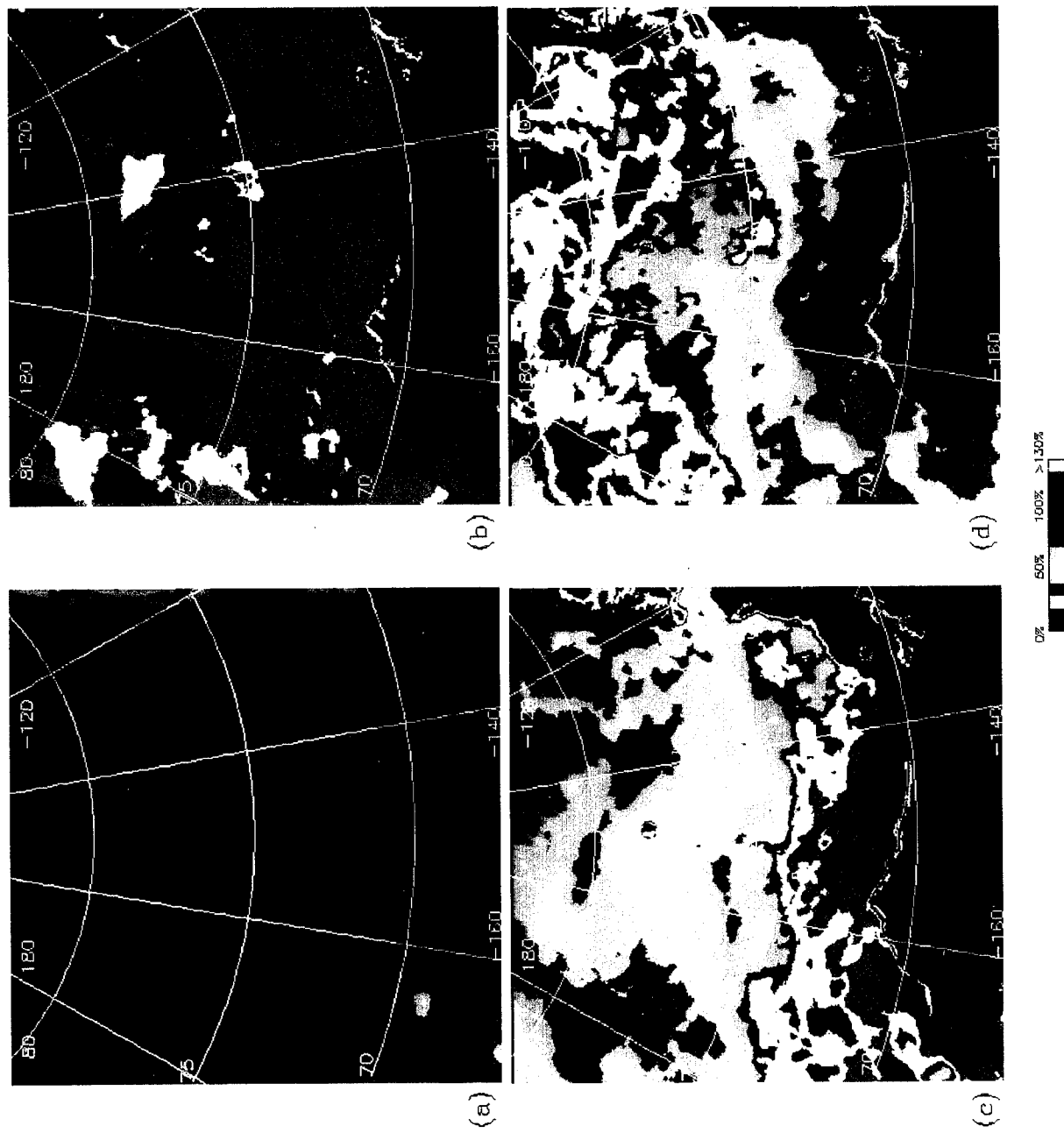


Fig. 20 — SSM/I data for the 8 Apr 89 Beaufort Sea test case, (a) total ice concentration, NASA algorithm, (b) total ice concentration, Navy algorithm, (c) multiyear ice concentration, NASA algorithm, (d) first-year ice concentration, NASA algorithm



(e)



(f)

Fig. 20 — Continued (e) ice type predominance chart, Navy algorithm and (f) 85 GHz H-pol brightness temperatures

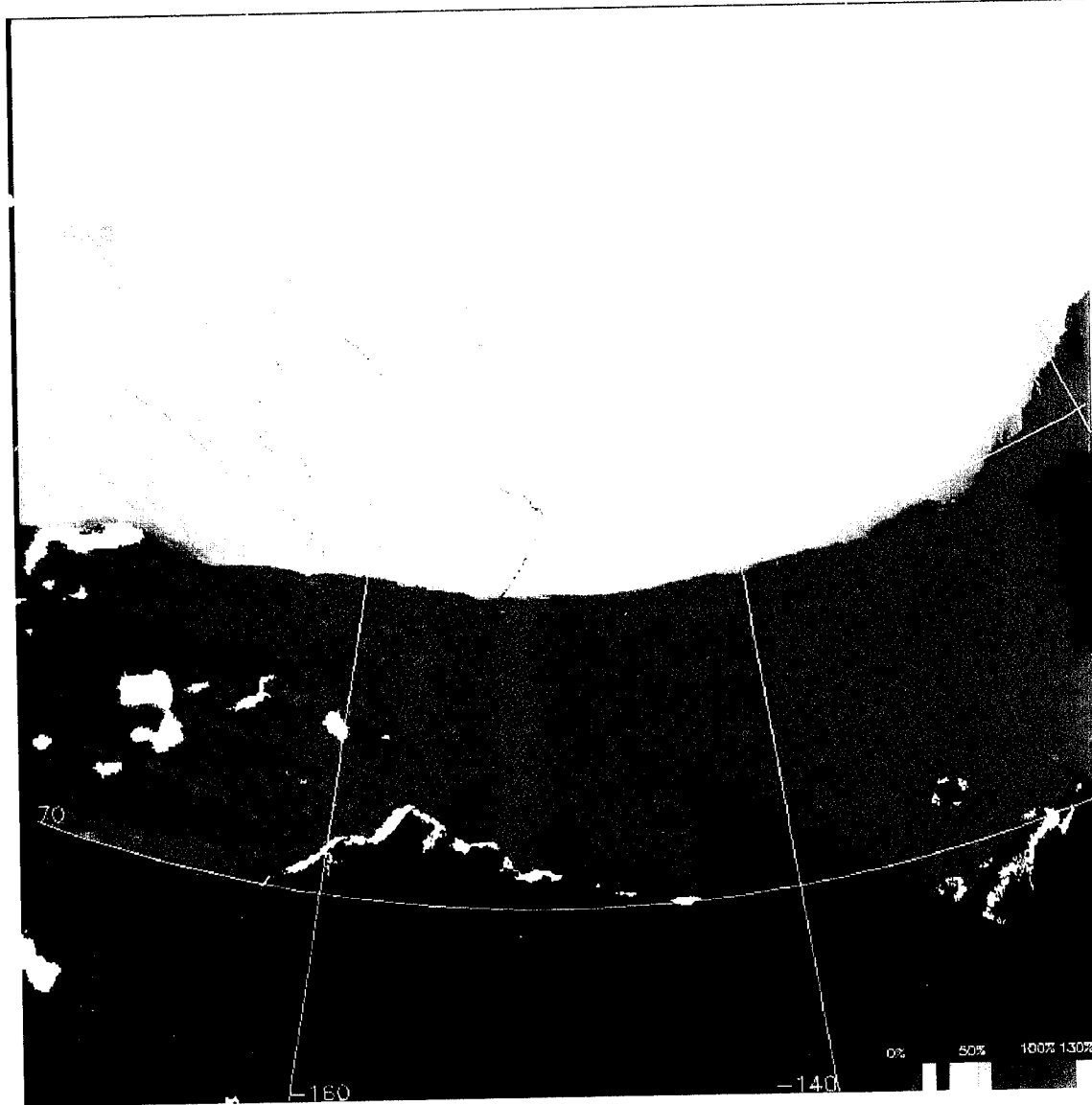


Fig. 21 — AVHRR/Navy total ice concentration composite for the 8 Apr 89 Beaufort Sea test case

## **7.0 Acknowledgments**

This work was sponsored by the Chief of Naval Operations (OP-096) under program element 0603704N, Satellite Ocean Tactical Applications Program. CDR D. Markham, program manager.

## 8.0 References

Burns, B. (1993). "Comparison of SSM/I Ice Concentration Algorithms for the Weddell Sea," *Annals of Glaciology* vol. 17, 344-350.

Cavalieri D. J. (1992). "NASA Sea Ice Validation Program for the Defense Meteorological Satellite Program Special Sensor Microwave Imager: Final Report," NASA Technical Memorandum 104559.

Chase J. R. and R. J. Holyer (1990). "Estimation of Sea Ice Type and Concentration by Linear Unmixing of Geosat Altimeter Waveforms," *Journal of Geophysical Research* vol. 95, c10, 18015-18025.

Emery W. J., M. Radebaugh, C. W. Fowler, D. J. Cavalieri, and K. Steffen (1991). "A Comparison of Sea Ice Parameters Computed from Advanced Very High Resolution Radiometer and Landsat Satellite Imagery and from Airborne Passive Microwave Radiometry," *Journal of Geophysical Research* vol. 96, c12, 22075-22085.

Grenfell T. C. and D. K. Perovich (1984). "Spectral Albedoes of Sea Ice and Incident Irradiance in the Southern Beaufort Sea," *Journal of Geophysical Research* vol. 89, c3, 3573-3580.

Lee T. F., S. Atwater, and C. Samuels (1993). "Sea Ice Edge Enhancement Using Polar-Orbiting Environmental Satellite Data," *Weather and Forecasting* vol. 8, 369-377.

Maslanik J. A. (1992). "Effects of Weather on the Retrieval of Sea Ice Concentration and Ice Type from Passive Microwave Data," *International Journal of Remote Sensing* vol. 13, no. 1, 37-54.

Massom R. and J. Comiso (1991). "The Detection of New Sea Ice and Surface Temperature Using Advanced Very High Resolution Radiometer and Special Sensor Microwave/ Imager Satellite Data," Proceedings of the 14th International Geoscience and Remote Sensing Symposium, vol. 2, Espoo, Finland, June 3-6, 1991, 791-795.

Poe G. A. (1990). "Optimal Interpolation of Imaging Microwave Radiometer Data," *IEEE Transactions of Geoscience and Remote Sensing* vol. 28, no. 5, 800-810.

Steffen K. and A. Schweiger (1989). "Sensitivity of Passive Microwave Sea Ice Concentration Algorithms to the Selection of Locally and Seasonally Adjusted Tie Points," Proceedings of the 12th International Geoscience and Remote Sensing Symposium, Vancouver, Canada, 773-776.

Steffen K. and A. Schweiger (1990). "A Multi-Sensor Approach to Sea Ice Classification for the Validation of DMSP SSM/I Passive Microwave Derived Sea Ice Products," *Photogrammetric Engineering and Remote Sensing* vol. 56, no. 1, 75-82.